

Porphyry Cu-Mo Stockwork Formation by Dynamic, Transient Hydrothermal Pulses: Mineralogic Insights from the Deposit at Butte, Montana

CELESTINE N. MERCER^{†,*} AND MARK H. REED

Department of Geological Sciences, 1272 University of Oregon, Eugene, Oregon 97403

Abstract

The systematic distribution of vein and alteration mineral assemblages in porphyry Cu deposits largely arises from changes in the temperature and pressure of fluids that traversed fractures throughout the hydrothermal system. Magmatic and hydrothermal minerals record the complex history of the fluctuating temperature and pressure regime as hydrothermal fluids transfer heat from their magmatic source to cold wall rock in response to lithostatic-to-hydrostatic pressure variations. We examine the thermal profile of the porphyry Cu-Mo deposit in Butte, Montana, by determining formation temperatures for magmatic and hydrothermal samples representing different time frames and depths within the deposit, in context with sample pressure estimates. We use three independent mineral thermobarometers: Ti in quartz, Zr in rutile, and X_{Mg} -Ti in biotite, from which we estimate that final dike injection temperature, and hence the initial magmatic-hydrothermal fluid temperature, was $\sim 700^\circ\text{C}$ while the ambient host-rock temperature was $\sim 450^\circ$ to 500°C . We find a magmatic-hydrothermal continuum represented in hydrothermal veins, ranging from $\sim 710^\circ$ to $<440^\circ\text{C}$. Distinct mineral generations within vein samples consistently display large temperature ranges, spanning 50° to 250°C , capturing the transient thermal condition of the ascending aqueous fluids. Mineral precipitation temperatures within veins show the same range as those in accompanying envelopes, indicating at least partly contemporaneous formation of veins and envelopes. Hydrothermal veins of a single type show no systematic relationship between temperature and depth within the deposit, although different vein types show systematic temperature ranges as a function of depth. We observe anomalous crosscutting relationships indicating that porphyry vein formation temperatures fluctuated significantly within a single cubic centimeter parcel of rock from one vein-forming episode to another. We suggest that the thermal profile does not mimic domical isograds based on alteration mineral zones, but rather it mimics an irregular pattern following active fractures at any given time and evolves by discrete cycles of dynamic, transitory, high-temperature hydrofracturing, fluid release, and vein formation that overprints cooler host-rock temperatures.

Introduction

PORPHYRY Cu deposits are composed of large volumes of hydrothermally altered rock centered on porphyritic, silicic magmatic intrusions. They develop as components of calc-alkaline batholiths and arc volcanoes at convergent plate margins (Sillitoe, 1973, 2010; Tosdal and Richards, 2001; Richards, 2003) and include important resources of Cu, Mo \pm Au, and minor amounts of other metals (Re, Ag, Pd, Te, Se, Bi, Zn, and Pb; Seedorff et al., 2005; Sinclair, 2007; Singer et al., 2008). Mid- to upper-crustal magma chambers are the precursors to volatile-rich felsic magmas that concentrate sulfur and metals into porphyry stocks or cupolas at about 1- to 5-km depth (Seedorff et al., 2005; Sillitoe, 2010). Fluid overpressurization within the crystallizing cupola leads to hydrofracturing of the overlying crust, intrusion of porphyritic dikes, and expulsion of metal-rich aqueous fluids that form a vein stockwork. High overall vein formation temperatures (550° – 700°C), transient lithostatic-to-hydrostatic pressures, and potassic alteration dominate early porphyry system veins, whereas late veins indicate declining temperatures, hydrostatic pressures, sericitic alteration, and waning fluid flux (e.g., Brimhall, 1977; Bowman et al., 1987; Redmond et al., 2004; Field et al., 2005; Seedorff et al., 2005; Rusk et al., 2006, 2008c; Reed and Palandri, 2010; Sillitoe, 2010; Reed et al., 2013).

The physicochemical evolution of hydrothermal fluids, and the resulting diversity of mineralization, in part reflects the evolution of the system's thermal profile through space and time. An intuitive underlying assumption in porphyry Cu genetic models is that the orebody shape, which is defined by the distribution of metals and alteration minerals, is a proxy for the system's thermal profile. This thermal profile is generally portrayed by gently curving concave isotherms that surround intrusions hosted by pervasively heated rock (e.g., Seedorff et al., 2005; Rusk et al., 2008c; Sillitoe, 2010). However, metasomatic isograds after which the character of the thermal profile has been inferred do not reflect pervasive alteration, but only alteration in centimeter-scale vein envelopes spaced meters to tens of meters apart. Mineralization is only truly pervasive where stockwork veinlets are so tightly spaced that their alteration envelopes overlap, leaving no unaltered wall rock (Roberts, 1975).

In this study, we conduct a detailed textural and geochemical survey of igneous and hydrothermal samples from the porphyry Cu-Mo deposit at Butte, Montana, to help define the space-time evolution of the thermal profile. Specifically, we apply three independent mineral thermobarometers: Ti in quartz (Thomas et al., 2010; Huang and Audétat, 2012), Zr in rutile (Tomkins et al., 2007), and X_{Mg} -Ti in biotite (Henry et al., 2005), in context with scanning electron microscopy (SEM) cathodoluminescence (CL) and backscattered electron (BSE) textural observations to better characterize the thermal profile. We evaluate whether rock that hosts the porphyry system was heated pervasively as previously envisioned, or whether

[†] Corresponding author: e-mail, cmercer@usgs.gov

^{*} Present address: U.S. Geological Survey, Denver Federal Center, Box 25046, MS 973, Denver, Colorado 80225.

high temperatures were attained only near vein-forming fractures. We also assess whether the thermal profile defines a single, major high-temperature fluid release followed by progressive cooling (e.g., Cathles and Shannon, 2007) or whether it evolved more dynamically through repeated, transient episodes of high-temperature fluid release.

Geologic background

The porphyry deposit at Butte, Montana, is hosted by the 77 to 75 Ma Butte Granite (e.g., Lund et al., 2002; Dilles et al., 2003), the volumetrically dominant pluton of the Boulder batholith (e.g., Smedes et al., 1973). The Butte Granite is remarkably homogeneous throughout the district (Doe et al., 1968; Smedes et al., 1973; Tilling, 1973; du Bray et al., 2012) and thereby provides a chemically uniform host-rock framework within which to evaluate features of the Butte deposit itself. Within the Boulder batholith, quartz porphyry dikes that cut the Butte Granite are unique to the Butte mining district (Figs. 1, 2A). The source stock from which the dikes emanate is not well constrained, however, the deepest drill holes (2 km) intersect a porphyry-rich zone in the center of the district that may be the uppermost extent of a parental cupola. Brimhall (1973) first recognized the Steward porphyry dikes as contemporaneous with porphyry mineralization (66–64 Ma; Lund et al., 2002; Dilles et al., 2003), and Meyer et al. (1968) recognized that the Modoc porphyry plug post-dates porphyry mineralization (64–63 Ma; Dilles et al., 2003;

Lund et al., 2005). The genetic link between the dikes and porphyry mineralization is indicated by the occurrence of chalcopyrite-bearing biotite breccias along dike borders (Brimhall, 1973) and dike apices that stream into biotite crackle veinlets, which in turn emanate from the dikes and constitute the earliest Cu mineralization (Reed et al., 2013).

Patterns of alteration and ore mineralization at Butte have been well documented (e.g., Meyer et al., 1968; Brimhall, 1973; Roberts, 1975; Rusk et al., 2008b; Reed et al., 2013). In the core of the district, early alteration includes characteristic biotite replacing host-rock hornblende (Roberts, 1975). Outside the core of the district, the intensity of this alteration gradually wanes to unaltered Butte Granite. Roberts (1975) described the hornblende biotitization as “pervasive,” although he recognized that it is controlled by the distribution of early quartz veins and biotite crackles. Pre-Main Stage Cu and Mo mineralization lies in two zoned domes that are ~2 km in diameter (Reed et al., 2013). The extent of the Anaconda and Pittsmtom domes are defined by magnetite-bearing vein zones and Mo-grade contours (Fig. 2). Both the Anaconda and Pittsmtom domes have typical porphyry-style concentric, overlapping alteration zones around centimeter-scale stockwork veins. A 1.2-km bulb-shaped zone of pyrite-quartz veins with pervasive gray sericitic (GS) alteration separates these two domes and extends downward more than 2 km. All three of these features are superimposed within a porphyry dike swarm (Fig. 2A).

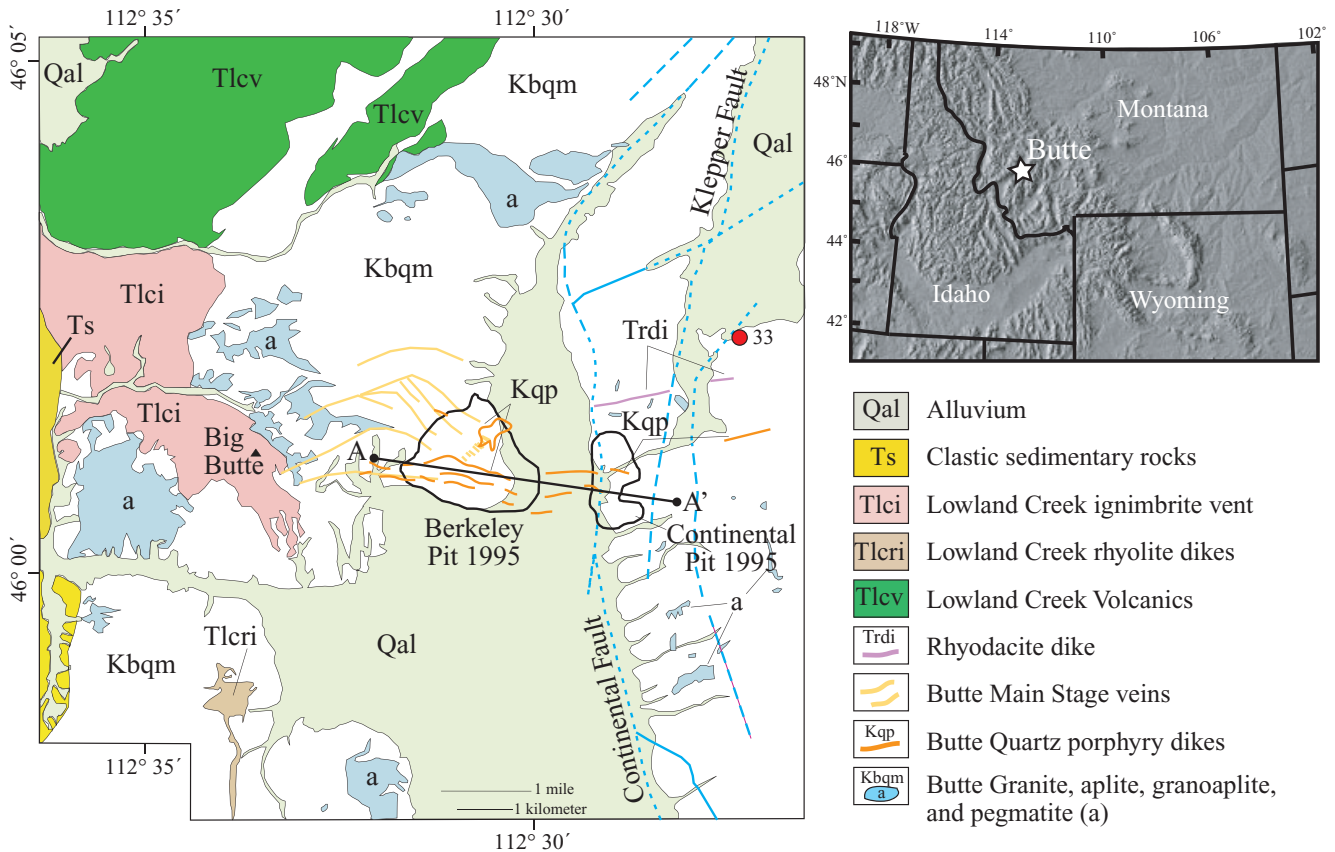


FIG. 1. Map showing the location and regional geologic setting of the Butte district (modified from Rusk et al., 2008c). Line A-A' denotes cross section in Figure 2. Red circle shows location of fresh Butte Granite sample (sample 33), described in Table 1.

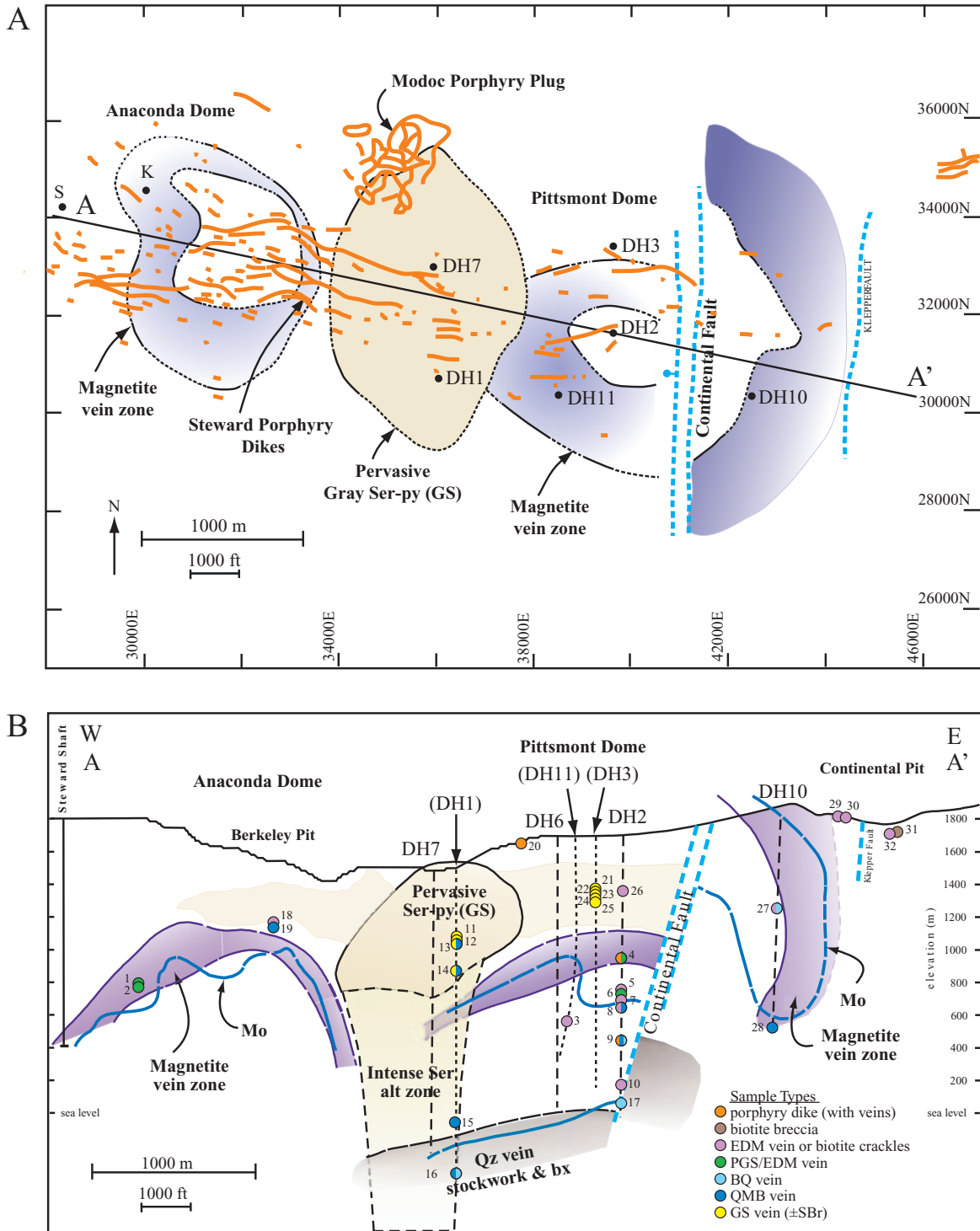


FIG. 2. Map and cross section showing the distribution of porphyry dikes, pre-Main Stage mineralization, and sample locations. (A). The subsurface trace of porphyry dikes at all depths is shown projected to the surface with orange lines. The subsurface position of pre-Main Stage mineralization centers is shown in purple for the Anaconda and Pittsmon dome Cu centers. A zone of pervasive sericitic alteration, shown in yellow, separates the two subsurface porphyry Cu mineral centers. Deep drill holes (DH) sampled in this study are numbered. The locations of the Steward (S) and Kelly (K) mine shafts are also shown. (B). West-east cross section (A-A') of pre-Main Stage porphyry Cu-Mo mineralization at Butte. The Anaconda and Pittsmon domes are defined by zones of abundant magnetite veins (shaded purple) and by Mo grade contours (blue lines). The Continental fault displaces the Pittsmon dome upward by ~1,300 m. Dashed lines indicate drill holes and mine shafts (those in parentheses indicate holes projected into this cross section). Colored circles show locations of samples analyzed for this study. Circles with multiple colors represent samples that contain crosscutting veins representative of different vein types. Map numbers correspond to sample numbers and descriptions in Table 1. Abbreviations are explained in Table 1.

A single magmatic fluid apparently produced the zoned domes as pressure, temperature, and pH conditions evolved during its ascent (Rusk et al., 2008c; Reed et al., 2013). The innermost zone in the Pittsmt dome includes barren quartz (BQ) veins with minor molybdenite and K-feldspar alteration. BQ veins grade upward and outward into a zone of quartz-molybdenite (QMB) veins which generally lack alteration envelopes. QMB veins cut veins of the next outward zone, consisting of quartz-chalcopyrite-pyrite veins with early dark micaceous (EDM) alteration envelopes that contain biotite, K-feldspar, sericite, and andalusite (Meyer, 1965; Brimhall, 1977). Early dark mica-dominant alteration grades upward and outward into abundant quartz-chalcopyrite-magnetite veins with pale-green sericitic (PGS) alteration envelopes composed of sericite, K-feldspar, and chlorite (Rusk et al., 2008c; Reed et al., 2013). EDM and PGS veins are both cut by BQ and QMB veins in the Anaconda and Pittsmt domes. Above the PGS zone is a zone that contains sparse quartz-pyrite-chalcopyrite veins with chlorite, sericite, and K-feldspar alteration envelopes (Geiger et al., 2002; Rusk et al., 2008c; Reed et al., 2013). Pyrite-quartz veins with GS alteration in the central bulb cut all other pre-Main Stage vein types. The outermost propylitic alteration zone contains K-feldspar, sericite, chlorite, epidote, sphalerite, and galena (Rusk et al., 2008c; Reed et al., 2013). Individual veins from any given zone reflect one or more episodes of fracturing, dilation, dissolution, and mineralization (Rusk and Reed, 2002). Igneous rocks, stockwork veins, and associated alteration at Butte have been well described and we refer readers to earlier works for further descriptions (e.g., Meyer et al., 1968; Brimhall, 1973, 1977; Roberts, 1975; Seedorff et al., 2005; Rusk et al., 2008c; du Bray et al., 2012; Reed et al., 2013).

Methods

Sample selection

We described and analyzed 33 samples from the Butte deposit, including igneous rocks, transitional magmatic-hydrothermal rocks, and hydrothermal stockwork veins. Igneous samples include fresh Butte Granite, Steward porphyry dikes, and the Modoc porphyry plug (Table 1, Figs. 1, 2). Transitional samples include biotite breccias from the margin of porphyry dikes and biotite crackles that emanate away from biotite breccias (Table 1, Fig. 2B). Most samples are pre-Main Stage stockwork vein types, including early dark micaceous (EDM), PGS, BQ, QMB, and GS (Table 1, Fig. 2B) and are from deep drill holes in the Pittsmt dome and the adjacent pervasive sericitic alteration zone in the center of the district at depths of 350 to 2,070 m below the surface. The deepest core samples represent the quartz vein stockwork with abundant porphyry dikes that are interpreted to be from near the top of the inferred cupola. Several samples of the Pittsmt dome are from the Continental and Berkeley pits and samples of the Anaconda dome are from underground drill holes at depths of 400 to 1,000 m below the surface.

SEM analyses

We conducted SEM imaging at the University of Oregon using an FEI Quanta 200 FEG scanning electron microscope equipped with an Oxford Instruments cathodoluminescence

(CL) detector and a Thermo SDD energy dispersive spectrometer detector. Polished 200- μm -thick sections were carbon coated (15–20 nm) and analyzed at 10 keV with a beam current of 0.5 to 5 nA for quartz, and 15 to 20 keV with a beam current of 2 to 8 nA for rutile and zircon. We collected more than 300 SEM-CL images of igneous and hydrothermal quartz with corresponding SEM-backscattered electron and secondary electron images. The CL image brightness of quartz is a function of operating conditions such as carbon coat thickness, beam conditions, bias, and gain, which we kept nominally constant except for the beam current, which we had to change depending on the luminosity of the quartz (Rusk et al., 2006). For the following discussion, relative CL brightness is described as CL-black, CL-dark, CL-gray, and CL-bright. We identified rutile and zircon using SEM-energy dispersive spectrometry and collected over 100 SEM-BSE images of these minerals.

Electron microprobe analyses

Trace element concentrations in quartz and rutile were measured at the University of Oregon using a Cameca SX-100 electron microprobe operated using two setups individually optimized for Ti in quartz and Zr in rutile. Quartz was analyzed using a 15-keV accelerating potential, a 200-nA beam current, and a 20- μm spot size (selected to average alteration caused by Ti diffusion; see mineral thermobarometry section). Ti was measured simultaneously on two spectrometers with LPET and PET crystals while Fe, K, and Al were measured on the remaining spectrometers. The “aggregate intensity” technique (Donovan et al., 2011) was applied using Probe for electron microprobe microanalyzer (EPMA) software to improve Ti counting statistics. Ti, Fe, K, and Al were counted for 600 s on-peak and 600 s off-peak. Synthetic rutile was used as a standard for Ti, synthetic magnetite was used for Fe, and natural orthoclase was used for K and Al. To reduce systematic continuum artifact errors, a matrix “blank” correction was applied to Ti data using a synthetic quartz standard as a Ti-free blank (Donovan et al., 2011). Detection limits (99% confidence) achieved on spot analyses are 4 ppm for Ti, 12 ppm for Fe, 11 ppm for K, and 6 ppm for Al. We avoided analyzing quartz within 200 μm of rutile needles to avoid excitation of Ti atoms by Bremsstrahlung radiation and/or secondary fluorescence (e.g., Bastin et al., 1984; Wark and Watson, 2006; Llovet et al., 2012), and consequent erroneously high Ti concentrations in quartz contaminated by rutile were easily identified and eliminated. One-sigma analytical errors on individual Ti-in-quartz analyses range from 1.5% at high Ti concentrations (10s of ppm) to 10% at 16 ppm Ti. As Ti concentrations approach 0 ppm the analytical errors grow exponentially with an error of ~50% at the detection limit of 4 ppm Ti.

Rutile was analyzed using a 15-keV accelerating potential, a 200-nA beam current, and a <1- μm spot size, which was required because some analyzed crystals were very small (<5 μm). Zr was measured simultaneously using two spectrometers with LPET and PET crystals while Fe and W were measured on one spectrometer, and Nb and Ta were measured on the remaining spectrometers. The “aggregate intensity” technique (Donovan et al., 2011) was also applied to improve Zr counting statistics. Zr, Ta, and Nb were counted for 300 s

TABLE 1. Sample Locations and Types

Location	Map no.	Sample no.	Location description	Depth below surface (m)	Elevation (m)	Host rock	Vein/alteration type
<u>West of CF</u>							
Anaconda	1	10772-32a	Kelly Shaft, 3400' level	1,037	763	BG	Qz-py-cp//PGS/EDM
Anaconda	2	10778-6	Kelly Shaft, 3400' level	1,037	763	BG	Qz-mt//PGS/EDM
Pittsmont	3	11185-3771	DH 11	1,150	553	BG	Qz-cp//EDM cut by qz-cp-py//NA
Pittsmont	4	11135-2470	DH 2	753	965	Steward ppy	Qz-py-cp//PGS
Pittsmont	5	11135-3481	DH 2	1,061	657	BG	Qz-py-cp//EDM
Pittsmont	6	11135-3568	DH 2	1,088	630	BG	Qz-py-cp//PGS/EDM
Pittsmont	7	11135-3586	DH 2	1,093	625	BG	Qz-py-cp//EDM
Pittsmont	8	11135-3597	DH 2	1,097	622	BG	Bi crackles cut by qz-mb//NA
Pittsmont	9	11135-2-4209	DH 2	1,283	435	Steward ppy	Qz-mb//NA cut by barren qz//NA
Pittsmont	10	11135-5051	DH 2	1,540	178(26)	BG	Qz-py-cp//EDM
<u>Pervasive GS zone</u>							
Central GS zone	11	10969-1571c	DH 1	479	1,217	BG	Py-qz//GS/SBr
Central GS zone	12	10969R-2075	DH 1	633	1,063	BG	Py-qz//GS
Central GS zone	13	10969-2101	DH 1	641	1,055	BG	Py//GS cut by qz-mb-py//NA
Central GS zone	14	10969-2665	DH 1	813	884	BG	Py-qz-op//GS cut by qz-mb-py//NA
Central GS zone	15	10969-5699	DH 1	1,738	-41	aplite	Qz-mb//NA
<u>Quartz vein stockwork</u>							
Central	16	10969-6804	DH 1	2,074	-378	aplite	Qz-mb//NA cut by barren qz//NA
Pittsmont	17	11135-5461	DH 2	1,665	53(-1,247)	aplite	Barren qz//NA
<u>Shallow GS</u>							
Anaconda	18	F2033-488	DH F2033	402	1,168	BG	Qz-py-cp//EDM
Anaconda	19	F2033-513	DH F2033	405	1,165	BG	Qz-mb//NA cut by qz-mb//NA
Pittsmont	20	11067-1	5480 bench	0	1,670	Modoc ppy	None
Pittsmont	21	11148-1141	DH 3	348	1,372	BG	Py-qz//GS/SBr
Pittsmont	22	11148-1169.4	DH 3	356	1,364	BG	Py-qz//GS/SBr
Pittsmont	23	11148-1197	DH 3	365	1,355	BG	Py-qz//GS/SBr
Pittsmont	24	11148-1293	DH 3	394	1,326	BG	Py-qz//GS/SBr
Pittsmont	25	11148-1300	DH 3	396	1,324	BG	Py-qz//GS/SBr
Pittsmont	26	11135-1150	DH 2	351	1,368	BG	Qz-py-cp//EDM
<u>East of CF</u>							
Pittsmont	27	11172-1847	DH 10	563	1,247(-53)	BG	Bi crackles cut by barren qz//NA
Pittsmont	28	11172-4247	DH 10	1,295	515(-785)	BG	Qz-mb//NA
Pittsmont	29	BUR-03-213	6080 bench	0	1,853(553)	BG	Bi crackles
Pittsmont	30	BUR-03-214	6080 bench	0	1,853(553)	BG	Qz-py//EDM
Pittsmont	31	BU96MR-11	5680 bench	0	1,731(431)	BG	Bi breccias
Pittsmont	32	BUR98-13	5480 bench	0	1,670(370)	BG	Bi crackles
Pittsmont	33	BU-214	Road cut, 46°02'26"N 112°27'25"W	0	2,072(772)	BG	Fresh

Notes: Map numbers correspond to sample labels in Figures 1 and 2B; elevation of samples that lie east of the Continental fault have been fault-corrected and are shown in parentheses next to present-day elevations; abbreviations: BG = Butte Granite, CF = Continental fault, DH = drill hole, EDM = early dark micaceous, GS = gray sericitic, NA = no alteration, PGS = pale green sericitic, SBr = sericite with remnant biotite, bi = biotite, cp = chalcopyrite, mb = molybdenite, op = open, ppy = porphyry, py = pyrite, qz = quartz

on-peak and 300 s off-peak. Fe was counted for 120 s on-peak and 120 s off-peak, and W was counted for 180 s on-peak and 180 s off-peak. Synthetic zircon was used as a Zr standard, synthetic magnetite was used for Fe, and pure metals were used for W, Nb, and Ta standards. Interference corrections were required for the Zr $L\alpha$ and Ta $M\alpha$ lines. Matrix "blank" corrections were applied for both Zr and Ta data using a synthetic TiO_2 standard as a Zr-free blank (Donovan et al., 2011). Calculated detection limits (99% confidence) on spot analyses are 16 ppm for Zr, 27 ppm for Fe, 130 ppm for W, 52 ppm for Nb, and 34 ppm for Ta. One-sigma analytical errors on individual microprobe analyses range from 1.5% at high Zr concentrations (100s of ppm) to 10% at ~50 ppm Zr. As for Ti

errors, analytical error grows exponentially as Zr concentrations approach 0 ppm with an error of ~50% at the detection limit of 16 ppm Zr.

We made no new analyses of biotite, but compiled chemical analyses from Zhang (2000) and Roberts (1975). We supplemented these analyses with additional biotite analyses by D.A. Soule (unpub.) who used a Cameca SX-50 electron microprobe at the University of Oregon.

Mineral thermobarometry

Ti-in-quartz thermobarometry: We employed the experimentally calibrated thermobarometers of Thomas et al. (2010) and Huang and Audétat (2012) to calculate quartz precipitation

temperatures. We assumed a pressure of 250 MPa for isobaric calculations involving igneous quartz and veins that formed near-lithostatic pressure (biotite crackles, EDM, BQ, and QMB), and 70 MPa for veins that formed near-hydrostatic pressure (PGS and GS) in accord with Butte fluid inclusion barometry results (Rusk et al., 2008c). Rutile is not present in granitic quartz, and there are no coexisting Fe-Ti oxides with which to calculate the activity of TiO_2 (a_{TiO_2}) for the porphyry dikes (e.g., Ghiorso and Evans, 2008). Consequently, we assumed an a_{TiO_2} of 0.5 by analogy to similar silicic magma systems for which a_{TiO_2} was determined by equilibria among coexisting Fe-Ti oxides (Wark et al., 2007) and the experimentally determined TiO_2 saturation model for rhyolite (Hayden and Watson, 2007). While rutile “needles” are present in all porphyry quartz phenocrysts, which suggests rutile saturation ($a_{\text{TiO}_2} = 1.0$), the porphyry magma was unlikely to be saturated with rutile due to its low bulk TiO_2 content of ~0.20 wt % (Hayden and Watson, 2007; Dilles, pers. commun.). Consequently, we infer that these randomly oriented rutile needles grew by localized diffusion of Ti during subsequent cooling and exsolution (Cherniak et al., 2007b), and we carefully avoided analyzing quartz within 200 μm of rutile needles and associated radially cylindrical Ti depletion zones. As with granitic quartz, we used an a_{TiO_2} of 0.5 for the porphyry quartz calculations. Rutile needles and blocky rutile occur in biotite breccias, biotite crackles, and all hydrothermal veins. We interpret the rutile needles in hydrothermal quartz to reflect regions of locally exsolved Ti due to cooling of the samples, however, blocky rutile grains are routinely intergrown with hydrothermal quartz and other alteration minerals and are thus interpreted to be hydrothermal, so we used an a_{TiO_2} of 1.0 in all calculations for hydrothermal quartz. Assuming an a_{TiO_2} of 1.0 provides a minimum temperature estimate, whereas using an a_{TiO_2} of 0.5 yields a calculated temperature ~80°C higher.

Ti is known to diffuse ~15 μm in quartz at 600°C over a million years (Cherniak et al., 2007b), which can alter original Ti concentrations and thus the significance of calculated temperatures. By using a microprobe beam spot size of 20 μm , we average the diffusional alteration of Ti concentrations. Therefore, we consider the effects of diffusion negligible over the 1- to 2-m.y. porphyry lifespan, a duration based on Ar-Ar and U-Pb dating (Lund et al., 2002; Dilles et al., 2003).

Huang and Audétat (2012) have demonstrated experimentally that the growth rate of quartz affects the concentration of Ti in quartz. We address the implications of variable quartz growth rates for our samples in the discussion below.

Zr-in-rutile thermobarometry: We calculated hydrothermal rutile precipitation temperatures using the experimentally calibrated thermobarometer of Tomkins et al. (2007). When possible, analyses of hydrothermal rutile grains in veins and alteration envelopes were acquired near (within ~1–2 mm) the locations of analyzed quartz. As with quartz, we assumed a pressure of 250 MPa for isobaric calculations involving veins that formed near-lithostatic pressure (biotite breccias, biotite crackles, EDM, BQ, and QMB), and 70 MPa for veins that formed near-hydrostatic pressure (PGS and GS) following results from Rusk et al. (2008c). The equilibrium controlling Zr contents in rutile requires the coexistence of zircon and quartz (Tomkins et al., 2007). Zircon grains, mostly <30 μm

in size, were identified intergrown with hydrothermal quartz and rutile in veins and alteration envelopes in 60% of the samples. The sparse distribution and small grain size of zircons made it difficult to confirm its presence in all samples, but given that zircon has been recognized as a common accessory mineral in the Butte Granite (e.g., Lund et al., 2002), we find evidence for some hydrothermal zircons, and since essentially all silicic rocks ubiquitously contain zircon (e.g., Watson et al., 2006), we assume that all of our analyzed samples contain zircon. The consistent presence of quartz in all analyzed samples fixes the activity of SiO_2 to 1.0, making this thermobarometer quite robust (Ferry and Watson, 2007).

Precision of the geothermometer is most precise at ~510°C with a 2σ error of $\pm 28^\circ\text{C}$. At ~650°C the error is $\pm 32^\circ\text{C}$ and at the detection limit (~430°C) the temperature error approaches $\pm 50^\circ\text{C}$.

X_{Mg} -Ti-in-biotite thermometry: We used the empirical X_{Mg} -Ti-in-biotite geothermometer of Henry et al. (2005) to calculate igneous and hydrothermal biotite precipitation temperatures. Biotite from the Butte samples falls within the calibrated compositional and temperature range specified for the geothermometer ($X_{\text{Mg}} = 0.275\text{--}1.000$, $\text{Ti} = 0.04\text{--}0.60$ atoms per formula unit (apfu), $T = 480^\circ\text{--}800^\circ\text{C}$); however, they likely formed at slightly lower pressure (~250 MPa) than the calibration range (400–600 MPa). We calculated biotite formula on an anhydrous basis with 22 oxygens to determine the Ti apfu following Henry et al. (2005).

Errors arising from application of the biotite geothermometer relate to microprobe analytical uncertainties and the precision of the empirical fit reported by Henry et al. (2005). Precision of the geothermometer is estimated to be $\pm 24^\circ\text{C}$ in the 480° to 700°C range and $\pm 12^\circ\text{C}$ in the 700° to 800°C range.

Results

Igneous and hydrothermal quartz

Cathodoluminescent (CL) images were used to distinguish different generations of quartz precipitation within each sample, all of which were then analyzed for trace elements by electron microprobe. Consequently our analyses best portray the range of Ti concentrations within each sample (e.g., a particular quartz vein may contain one generation of quartz with ~50 ppm Ti and another generation with ~100 ppm Ti), but they do not reflect the frequency distribution of a given Ti concentration (i.e., our analyses give no information about what proportion of the vein may contain 50 ppm Ti vs. 100 ppm). In addition, we distinguished “compositional zones,” which are typically 50 to 1,000 μm in width and result from extrinsic physicochemical changes during quartz growth (e.g., pressure, temperature, a_{TiO_2} , etc.), from “oscillatory zones,” which are generally <2 to 20 μm thick and result from intrinsic diffusion-controlled boundary layer effects (e.g., Shore and Fowler, 1996; D’lemos et al., 1997; Götze et al., 2001). Nearly all analyses represent the former, and we specify the few analyses that represent the latter.

Quartz in the host Butte Granite and porphyry dikes exhibits a variety of CL textures (Fig. 3). Butte Granite quartz grains are 0.5 to 3 mm in diameter and are always relatively CL bright compared to hydrothermal quartz, as observed by

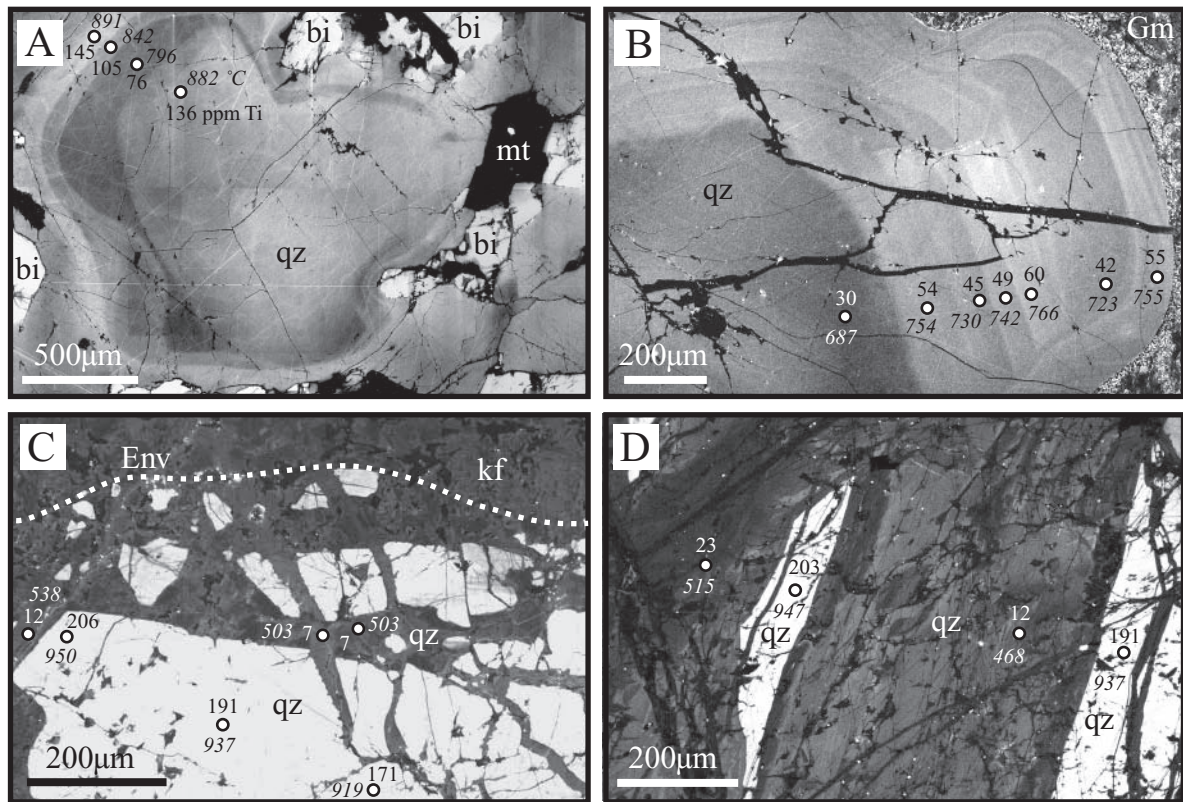


FIG. 3. Examples of cathodoluminescent textures preserved in igneous quartz. Quartz (qz) dominates these images unless otherwise marked: bi = biotite, kf = K-feldspar, mt = magnetite, Gm = groundmass, Env = envelope. Representative microprobe analyses are shown with Ti concentrations given in ppm (regular font), and corresponding isobaric temperature estimates ($^{\circ}\text{C}$) calculated using Huang and Audétat (2012) are shown in italics. (A). CL-bright plutonic quartz from Butte Granite (BU-214_Q5), center shows concentric bands resembling resorption/overgrowth bands in magmatic quartz phenocrysts, while upper left and right show interstitial quartz. (B). CL-bright porphyritic quartz “eye” from Modoc porphyry dike with prominent microcracks filled with CL-black hydrothermal quartz (11067-1_Q1). (C). Angular fragments of CL-bright quartz from the Butte Granite cemented together by CL-dark quartz in a shallow EDM vein (11135-1150_Q2), dotted line indicates edge of vein. (D). Angular fragments of CL-bright quartz from the Butte Granite cemented together by CL-dark quartz in a shallow GS vein (10969R-2075_Q1).

Rusk et al. (2006). Many large grains show CL-bright cores with rounded, alternating CL-gray and CL-bright concentric bands suggestive of resorption and overgrowth processes, whereas small grains of interstitial quartz are relatively monotonous and CL-gray (Fig. 3A). Boundaries between CL-bright and CL-gray zones are generally diffuse. Quartz phenocrysts from porphyry dikes are 0.5 to 7 mm in diameter and are characteristically rounded (i.e., resorbed). CL images reveal CL-gray cores surrounded by ~3 to 15 concentric, rounded to euhedral, alternating CL-gray and CL-bright growth bands (Fig. 3B). The boundaries between CL-gray and CL-bright bands are most diffuse near the core of the quartz phenocrysts. Nearly all granitic and porphyry quartz grains contain secondary CL-dark features that overprint primary, relatively CL-bright textures (i.e., hydrothermal quartz-filled microcracks that are relatively CL-dark; Fig. 3A, B). Angular fragments of CL-bright quartz from the Butte Granite are cemented by CL-dark hydrothermal quartz in many veins, particularly veins that formed at shallow levels (Fig. 3C, D).

Hydrothermal quartz displays a large variety of CL brightness and textures within individual samples and among sample types. We have divided these textures based on two

main observations. First, many samples show distinct generations of quartz that are recognizable by relatively sharp overgrowth rims, abrupt changes in CL textures, and distinctive Ti concentrations, and therefore formed by successive fluid-flow events (e.g., Rusk and Reed, 2002; Rusk et al., 2006). We carefully distinguish these generations when interpreting trace element data. Second, many samples show indistinct textural gradations in quartz that are either relatively monotonous or heterogeneous in CL-brightness and Ti concentration. Because there are no sharply contrasting, crosscutting, or superpositional CL characteristics to differentiate one generation of this type from another, we have grouped each of these indistinct generations within each sample together for trace element data interpretation.

Samples with distinct generations of quartz are shown in Figure 4. Biotite crackles that formed deep within the deposit display CL-dark, resorbed, rounded quartz cores that are overgrown by CL-bright quartz that also fills fine fractures (Fig. 4A). Many BQ and QMB veins contain wide (50–200 μm) CL-gray to CL-dark veinlets that cut original, brighter vein quartz (Fig. 4B). Boundaries of crosscutting veins are not always straight, and at a fine scale deviate along quartz grain

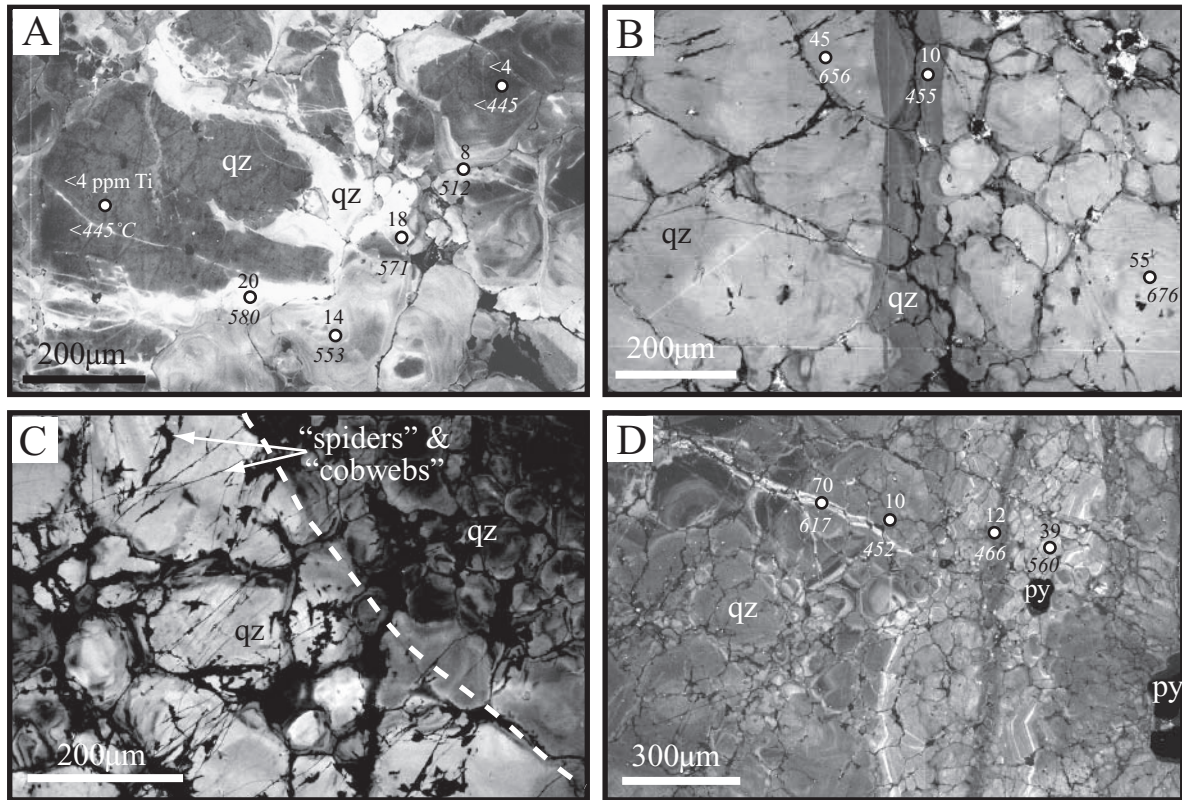


FIG. 4. Examples of cathodoluminescent textures in vein quartz that show distinct generations of quartz. Generations are distinguished by crosscutting relationships, abrupt changes in CL brightness, and overgrowth textures. Quartz (qz) dominates these images unless otherwise marked: py = pyrite. Representative microprobe analyses are shown with Ti concentrations given in ppm (regular font), and corresponding isobaric temperature estimates ($^{\circ}\text{C}$) calculated using Huang and Audéat (2012) are shown in italics. (A). Biotite crackle with rounded CL-dark quartz grains overgrown by CL-bright quartz that also fills small fractures (BUR-03-213_Q1). (B). CL-bright quartz-molybdenite vein cut by later stage CL-gray veinlet (11135-2-4209_Q1); note CL-gray quartz extends into fractures and along grain margins, as does another generation of CL-black quartz. (C). Contact (dashed line) between CL-dark EDM quartz vein cut by CL-bright barren quartz vein (11185-3771_Q5); note grains of both veins are cut and surrounded by “spiders and cobwebs” of CL-black quartz that represent a third quartz generation (Rusk and Reed, 2002). (D). GS vein with CL-gray quartz along vein margins (left and right) that is filled by CL-brighter quartz (right of center) and a small seam of CL-darker quartz; note enveloped pyrite and euhedral quartz growth bands, CL-dark grains overgrown by CL-brighter quartz, CL-bright grains overgrown by CL-darker quartz, and the CL-bright rim along the fracture that is perpendicular to the vein (upper left; 10969-2665_Q2).

boundaries and cracks within the preceding vein (Fig. 4B). Crosscutting relationships include CL-bright quartz that is cut by CL-dark quartz (Fig. 4B) and CL-dark quartz that is cut by CL-bright quartz. For example, a CL-gray EDM vein is cut by a later generation of CL-bright BQ (Fig. 4C), which is in turn cut by CL-black quartz that resembles “spiders and cobwebs” (Rusk and Reed, 2002). Many veins display a complex combination of overgrowths and crosscutting CL textures. For example, a GS vein, which shows heterogeneous CL-gray vein quartz (that envelopes pyrite) with euhedral overgrowths, is cut by a heterogeneous CL brighter vein (that also envelopes pyrite), that is in turn cut by a CL-gray veinlet (Fig. 4D, right of center). Nearly all quartz grains from every vein type display CL-black grain boundaries and CL-black “spiders and cobwebs” (Rusk and Reed, 2002).

CL textures indicate that some samples display indistinct generations of quartz (Fig. 5). Many BQ, QMB, and GS veins exhibit relatively monotonous CL-gray textures (Fig. 5A), whereas others display grains with heterogeneity in CL-brightness, both within grains and among grains (Fig. 5B,

C). Several deep and shallow quartz grains of all vein types preserve euhedral growth bands along vein edges (Fig. 5C) and along vein-parallel fractures within the vein (Fig. 4D). GS veins tend to have more quartz with euhedral growth bands than any other vein types, and these bands tend to occur as bands parallel to the fracture wall (Fig. 4D) rather than as single grains of zoned quartz that sit among monotonous or mottled quartz grains (Fig. 5C). However, not all quartz in GS veins contains euhedral bands. Most deep EDM veins contain CL-bright to CL-gray heterogeneous grains, some of which have thin ($5\ \mu\text{m}$) CL-bright semiconcentric bands (Fig. 5D). None of these CL textures is clearly diagnostic of a particular vein type.

Electron microprobe trace element analyses of quartz (Table 2) show that concentrations of Fe, Al, and K in different generations of quartz in individual samples are highly heterogeneous. As observed in other studies, Ti concentrations are relatively less heterogeneous and correlate positively with relative CL brightness for high-temperature ($>500^{\circ}\text{C}$) quartz (e.g., Müller et al., 2003; Landtwing and Pettke, 2005; Rusk

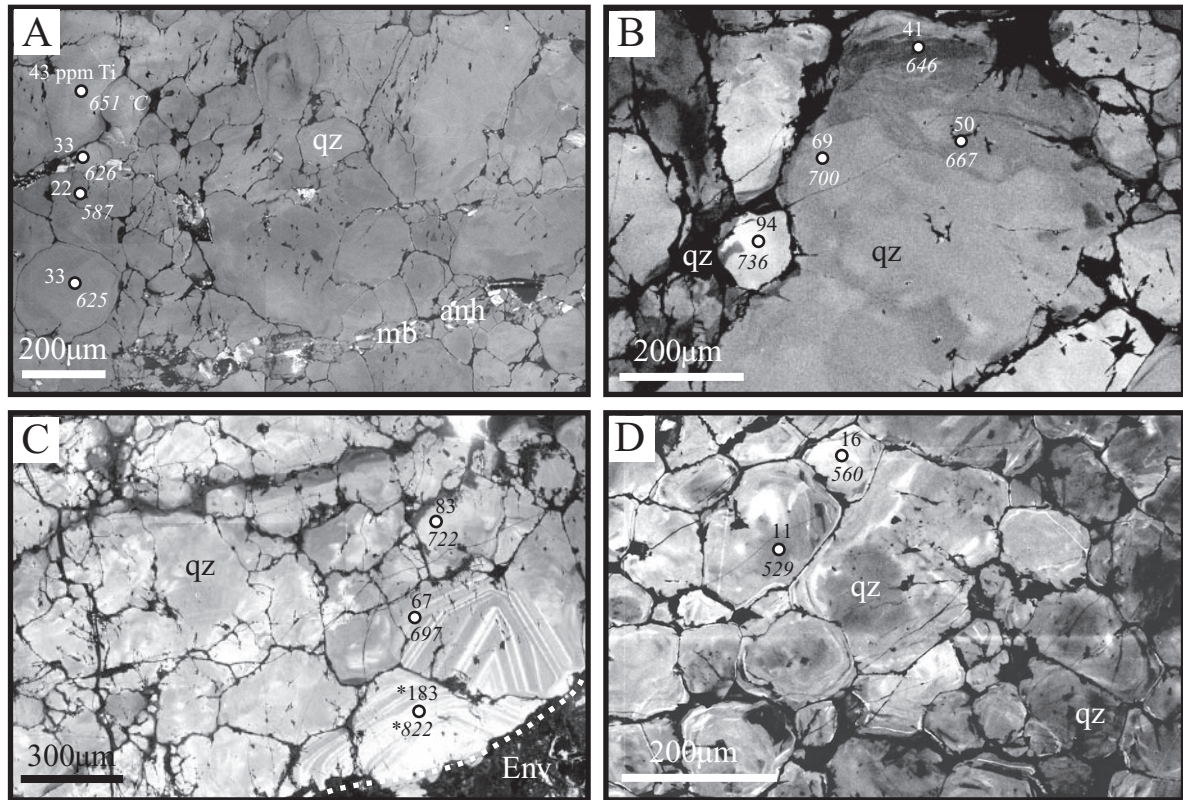


FIG. 5. Examples of cathodoluminescent textures in vein quartz that show indistinct generations of quartz with either monotonous or heterogeneous features (i.e., quartz for which there are no obvious crosscutting relationships, abrupt changes in CL brightness, or overgrowth textures). Note that we ignore CL-black “spiders and cobwebs” (Rusk and Reed, 2002) that overprint most pre-Main Stage porphyry and vein quartz. Images are dominantly quartz (qz) unless otherwise marked: anh = anhydrite, mb = molybdenite, Env = envelope. Representative microprobe analyses are shown with Ti concentrations given in ppm (regular font), and corresponding isobaric temperature estimates ($^{\circ}\text{C}$) calculated using Huang and Audétat (2012) are shown in italics. (A). QMB vein with monotonous CL-gray texture (11172-4247_Q2). (B). QMB vein with CL heterogeneity within and among quartz grains (10969-5699_Q2). (C). Deep BQ vein with blotchy quartz grains and CL-bright euhedral growth bands; *thin CL-bright oscillatory bands are thought to be formed from an intrinsic diffusion-controlled boundary layer effect (e.g., Shore and Fowler, 1996; D’lemos et al., 1997; Götze et al., 2001); dotted line indicates edge of vein (10969-6804_Q2). (D). Deep EDM vein quartz with grains of varying CL brightness (but no clear rims) (11185-3771_Q4).

et al., 2006, 2008a; Müeller et al., 2010). This consistent correlation, along with low Ti detection limits in CL-dark quartz, indicates that Bremsstrahlung radiation and/or secondary fluorescence did not hinder our Ti analyses. Concentrations of Al and K show a weak positive correlation, presumably owing to coupled substitution. Fe and K concentrations do not correlate with CL brightness nor with any other determined trace element abundance. Notably, Al concentrations do not correlate with Ti concentrations (Fig. 6) or with CL brightness, unlike some experimentally grown quartz that was used to calibrate the Ti-in-quartz thermobarometer (Huang and Audétat, 2012). However, individual quartz types do tend to show distinct, but overlapping ranges of Ti and Al concentrations. For example, Butte Granite quartz has the highest Ti concentrations (~50–160 ppm), but a limited range of lower Al concentrations (~55–320 ppm). Quartz phenocrysts from porphyry dikes contain relatively moderate concentrations of both Ti (~20–70 ppm) and Al (~125–465 ppm). Concentrations of Ti and Al in hydrothermal quartz from BQ and QMB veins encompass nearly the entire range defined by hydrothermal samples (~5–100 ppm Ti, ~30–3,675 ppm Al),

whereas those from EDM and PGS veins are generally limited to lower Ti concentrations (~5–40 ppm) and low to moderate Al concentrations (~30–370 ppm). Overall, GS vein quartz has the lowest Ti concentrations (~5–35 ppm) but spans the entire range from low to high Al concentrations (~15–3,330 ppm).

Comparison of Ti concentrations in quartz phenocrysts from Butte porphyry dikes relative to Ti-in-quartz isopleths and the revised thermobarometer of Thomas et al. (2010) for $a_{\text{TiO}_2} = 0.5$ are consistent with their growth in a relatively broad range of temperature and pressure conditions (Fig. 7). The effect of pressure on this thermobarometer is notable because the Ti isopleths are only moderately steep in terms of pressure and temperature (Fig. 7). Assuming that the Butte porphyry deposit formed at lithostatic to hydrostatic pressures (Fig. 7, gray shaded field) between 250 and 70 MPa (Tilling, 1973; Roberts, 1975; Dilles et al., 1999; Rusk et al., 2008c), application of the Thomas et al. (2010) calibration in the Butte pressure range indicates quartz phenocryst temperatures well below the water-saturated granite solidus (Holtz et al., 2001). These temperatures (Fig. 7, Table 2) are significantly cooler

TABLE 2. Microprobe Analyses of Trace Elements in Quartz and Calculated Ti-In-Quartz Temperatures

Sample no.	n	Ti (ppm)	Fe (ppm)	Al (ppm)	K (ppm)	Ti-in-quartz (°C)	
						Thomas et al. ¹	Huang & Audétat ²
Granite and porphyry quartz, CL-bright							
Fresh Butte granite quartz, CL bands							
BU-214_Q5	14	108(23)	25(15)	127(69)	15(8)	660(24)	844(31)
BU-214_Q9	10	111(43)	22(8)	87(21)	13(2)	669(39)	842(64)
Fresh Butte granite quartz, interstitial							
BU-214_Q10	6	58(10)	16	69(9)	13(6)	596(16)	760(21)
BU-214_Q4	3	81(5)	33(3)	146(34)	16(6)	632(6)	806(8)
BU-214_quartzA	3	74(2)	22(13)	189(114)	48	622(2)	794(3)
Butte granite quartz in vein wall or vein breccias							
11135-1150_Q1	3	73(2)	312(74)	461(612)	80(103)	620(3)	791(4)
11135-1150_Q2	4	171(55)	124(107)	218(51)	47(21)	712(49)	912(64)
F2033-488_Q1	2	124(26)	78(86)	315	107(71)	677(24)	866(32)
F2033-513_Q1	2	63(16)	46(33)	796(522)	26(12)	604(25)	770(32)
10969-2101_Q1	1	92	24	255	17	645	824
10969R-2075_Q1	5	176(31)	4,189(9221)	197(272)	123(166)	719(24)	921(32)
10969-2665_Q1	2	73(7)	62	161(54)	14(7)	621(9)	792(12)
Steward-type porphyritic quartz							
11135-2470_Q1	10	45(13)	145(87)	265(188)	78(51)	568(25)	724(32)
11135-2470_Q3	16	41(8)	21(9)	177(54)	46(53)	564(18)	718(23)
11135-2-4209_Q2	4	51(8)	21(9)	317(80)	36(14)	586(14)	747(18)
Modoc-type porphyritic quartz							
11067-1_Q1	20	48(10)	65(7)	220(41)	22(4)	578(20)	736(26)
11067-1_Q3-A	18	41(10)	65(59)	187(79)	74(29)	564(21)	723(33)
11067-1_Q3-B	15	40(9)	48(37)	170(26)	20(3)	562(23)	716(29)
Hydrothermal quartz, CL-gray veins							
Biotite crackles							
BUR-03-213_Q1	7	14(4)	53(39)	75(14)	22(14)	433(17)	551(22)
BUR-03-213_Q1-B	3	15(5)	33(10)	82(31)	23(16)	435(20)	554(25)
BUR-03-213_Q2 ³	5	29(16)	82(27)	107(40)	37(24)	445(14)	567(17)
EDM veins							
11185-3771_Q4	4	12(4)	16(3)	79(20)	MDL	423(20)	540(24)
BUR-03-214_Q1	7	9(3)	16(3)	49(29)	19(7)	414(39)	528(48)
BUR-03-214_Q3	5	MDL	15(2)	54(11)	32(17)	MDL	MDL
11135-5051_Q1	8	24(6)	52(60)	54(7)	21	467(20)	594(25)
11135-1150_Q1	4	10(7)	707(148)	145(20)	44(19)	405(43)	517(53)
11135-1150_Q2	3	9(3)	169(61)	145(28)	31(17)	401(19)	512(23)
F2033-488_Q1	11	24(12)	102(189)	1,579(952)	263(204)	460(36)	586(46)
PGS veins							
11135-2470_Q2b	13	16(10)	88(63)	194(142)	82(92)	395(35)	474(41)
11135-2470_Q5b	10	23(9)	25(8)	112(95)	75(92)	426(28)	512(33)
BQ veins							
11185-3771_Q3	9	53(15)	36(19)	131(58)	49(22)	526(21)	670(27)
11172-1847_Q2	4	56(7)	MDL	119(10)	MDL	532(11)	678(14)
11135-5461_Q1	8	63(16)	16(4)	158(31)	27(19)	540(22)	688(29)
11135-5461_Q2	8	80(12)	16(3)	169(68)	36(22)	562(13)	716(16)
11135-2-4209_Q3	7	24(12)	21	224(301)	11(1)	460(39)	587(49)
10969-6804_Q2 ³	5	88(55)	21	621(438)	69(117)	542(23)	690(29)
10969-6804_Q3	8	65(20)	MDL	190(145)	19(9)	543(26)	691(33)
QMB veins							
10969-5699_Q1	10	36(7)	20(11)	52(18)	25(29)	497(14)	632(18)
10969-5699_Q2	9	66(15)	45	105(91)	47(83)	545(20)	694(26)
10969-5699_Q3	8	39(11)	15(6)	52(11)	12(2)	502(19)	640(24)
10969-5699_Q4	5	69(21)	MDL	73(18)	MDL	547(30)	697(39)
11172-4247_Q1	8	17(4)	72(89)	1,066(1668)	24(17)	443(16)	564(20)
11172-4247_Q2	8	32(6)	18(6)	146(51)	25(9)	489(14)	622(18)

TABLE 2. (Cont.)

Sample no.	n	Ti (ppm)	Fe (ppm)	Al (ppm)	K (ppm)	Ti-in-quartz (°C)	
						Thomas et al. ¹	Huang & Audétat ²
10969-6804_Q1	9	52(20)	33(8)	694(1022)	17(6)	521(37)	664(47)
F2033-513_Q1	9	26(11)	114(153)	561(254)	70(127)	469(29)	597(36)
F2033-513_Q2	8	22(8)	111(179)	869(1026)	174(316)	459(24)	585(31)
11135-3597_Q1	9	24(8)	24(9)	139(48)	22(10)	464(24)	591(31)
11135-3597_Q2	9	32(19)	99(195)	220(245)	59(98)	479(46)	610(59)
11135-2-4209_Q1	7	41(9)	59	155(65)	15(5)	507(18)	645(23)
<u>GS veins</u>							
10969-2101_Q1	12	23(8)	115(202)	850(1261)	11(2)	425(29)	510(35)
10969R-2075_Q1	10	21(12)	69(89)	918(1062)	106(87)	420(39)	505(47)
10969R-2075_Q2 ³	6	11(5)	25(10)	202(338)	56(42)	381(28)	458(33)
10969-2665_Q1	7	18(13)	622(862)	1,000(1436)	170(290)	406(40)	487(48)
10969-2665_Q2	9	28(20)	103(62)	1,161(1206)	191(215)	420(39)	504(47)
Hydrothermal quartz, CL-dark veinlets/fracture fillings							
<u>Filling Modoc-type porphyritic quartz</u>							
11067-1_Q1_darkqz	5	7(1)	56(8)	159(69)	MDL	357(8)	422(17)
<u>Filling EDM veins</u>							
11135-5051_Q1	2	MDL	27(15)	52(17)	28	MDL	MDL
<u>Filling BQ veins</u>							
11185-3771_Q3	4	12(3)	33(14)	268(128)	71(50)	390(130)	468(15)
10969-6804_Q2	3	12(7)	12	1,096(1527)	126(162)	380(43)	456(51)
<u>Filling QMB veins</u>							
11172-4247_Q2	1	19	17	573	50	418	501
11135-2-4209_Q1	2	14(5)	473(31)	128(7)	14	395(23)	474(28)
Hydrothermal quartz, CL-dark grain boundaries							
<u>Grain edge in BQ veins</u>							
11185-3771_Q3	2	19(3)	20(4)	78(6)	MDL	451(9)	574(12)
11135-5461_Q1	1	16	MDL	114	9	439	560
11135-5461_Q2	1	36	14	263	9	498	634
10969-6804_Q2	1	7	MDL	103	12	389	497
10969-6804_Q3	1	6	MDL	494	15	385	491

Notes: Data are reported as averages of multiple microprobe analyses; samples with large standard deviations are highly heterogeneous; number in parentheses next to each analysis represents 1σ ; errors given in terms of least unit cited (e.g., 108(23) represents 108 ± 23); n = number of analyses, MDL = below 99% minimum detection limit, n/a = not applicable; see Table 1 notes for abbreviations

¹ The Ti-in-quartz thermobarometer calibration of Thomas et al. (2010) is not appropriate for igneous or hydrothermal samples from Butte

² The Ti-in-quartz thermobarometer calibration of Huang and Audétat (2012) provides reasonable temperature estimates for igneous quartz but must be interpreted with caution for hydrothermal samples as discussed in the text

³ Denotes analysis of high Ti CL-bright rim/zone; temperatures estimates above do not include these high Ti data

than expected, which suggests that either: (1) quartz porphyry phenocrysts within the porphyry dikes were formed at pressures several 100 MPa higher than expected, (2) the porphyry ore deposit formed much deeper than has been proposed, (3) the prevailing a_{TiO_2} was much lower than we assumed, (4) the Ti concentrations in quartz phenocrysts changed significantly after crystallization, (5) the Ti concentration did not equilibrate in quartz, and (6) the thermobarometer calibration of Thomas et al. (2010) may be in error. While it is possible that quartz phenocrysts formed at somewhat higher pressures, the pressures required to produce temperatures above the water-saturated granite solidus would imply dominantly mid-crustal quartz growth, which is plausible but not necessarily

expected. The presence of rutile needles within quartz phenocrysts indicates that the Ti content of the quartz changed locally (i.e., within $\sim 200 \mu\text{m}$ of a rutile needle) during cooling, and Ti diffusion likely redistributed Ti in quartz locally (i.e., $\sim 20 \mu\text{m}$) upon cooling, however, our dataset does not reflect these effects because of our choice in analytical methods. Independent evidence in support of possibilities (2), (3), (4), or (5) is lacking, and in parallel with similar findings of Wilson et al. (2012), we conclude that the thermobarometer calibration of Thomas et al. (2010) does not sensibly apply to the natural magmatic environment at Butte. By extension, the temperatures we calculate for quartz from the Butte Granite (Table 2) are unreasonably low and must also be in error.

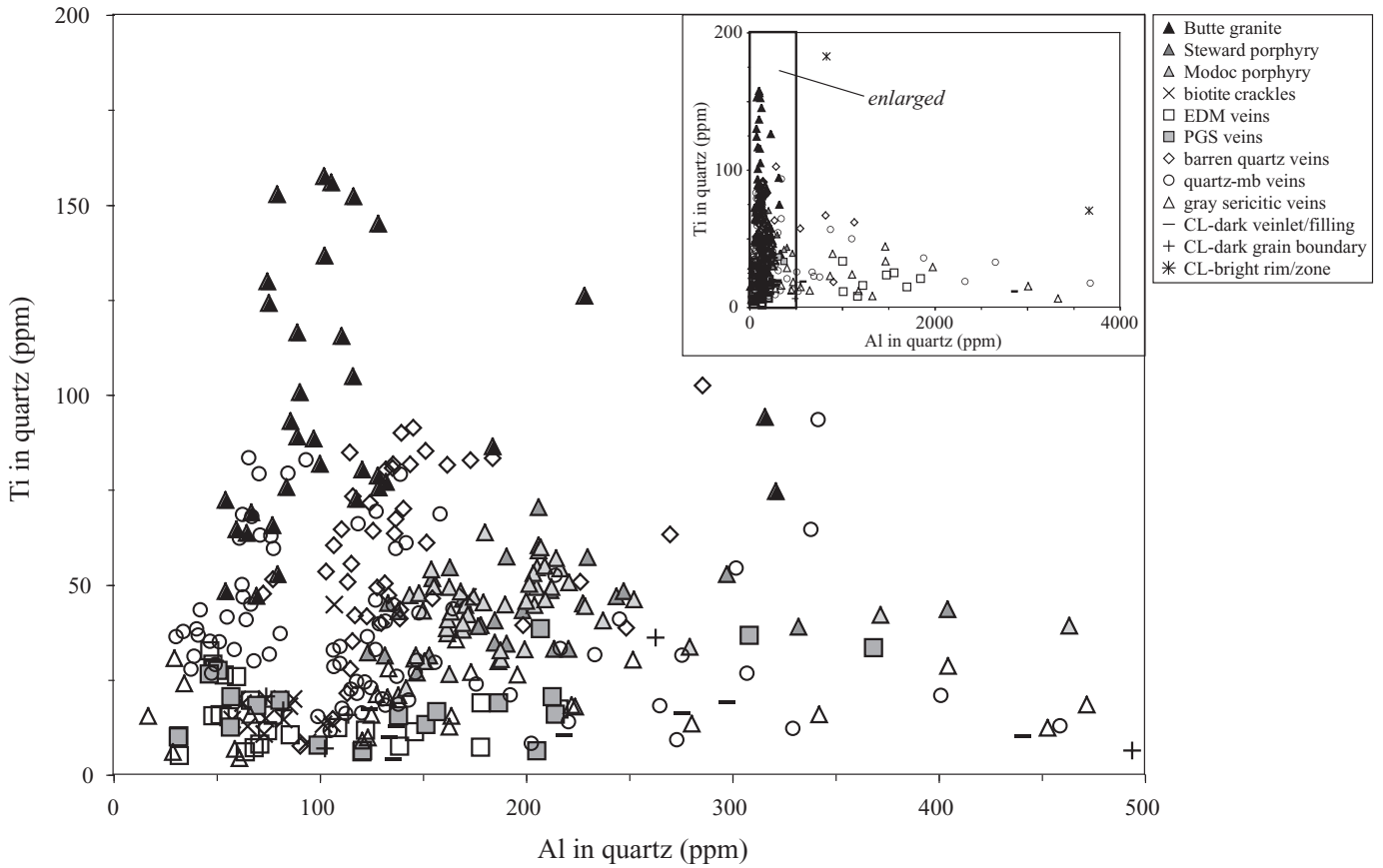


FIG. 6. Concentrations of Ti and Al in quartz. Inset shows the large range of Al concentrations in BQ, QMB, GS veins, and several analyses from EDM veins.

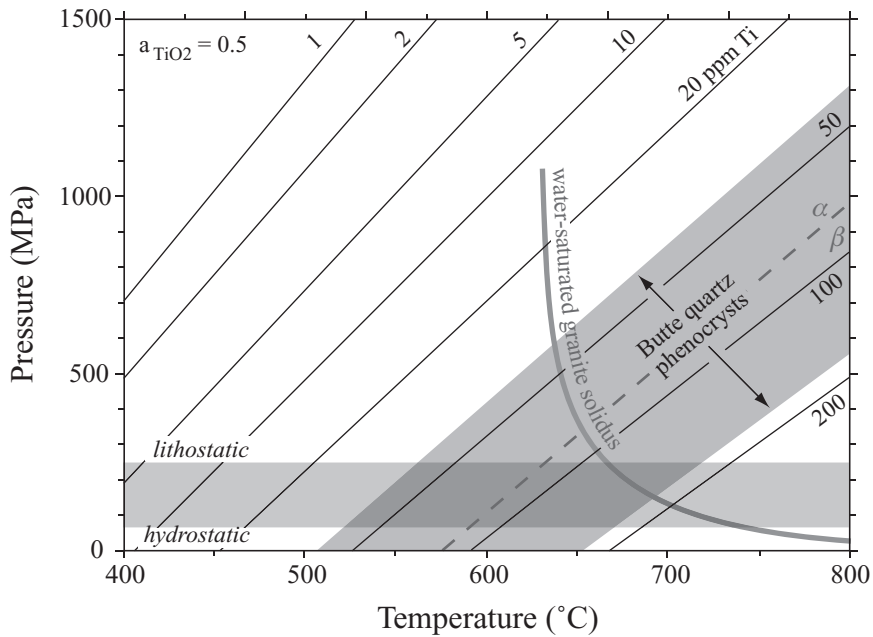


FIG. 7. Range of Ti concentrations in quartz phenocrysts from the Butte porphyry dikes is shown (gray shaded field) relative to Ti-in-quartz isopleths (black lines) and corresponding pressures and temperatures from the thermobarometer of Thomas et al. (2010) for an assumed a_{TiO_2} of 0.5. The experimentally determined haplogranite water-saturated solidus curve (Holtz et al., 2001) for an assumed a_{TiO_2} of 0.5. The experimentally determined haplogranite water-saturated solidus curve (Holtz et al., 2001) for an assumed a_{TiO_2} of 0.5. The experimentally determined haplogranite water-saturated solidus curve (Holtz et al., 2001) for an assumed a_{TiO_2} of 0.5. The experimentally determined haplogranite water-saturated solidus curve (Holtz et al., 2001) for an assumed a_{TiO_2} of 0.5. Also shown is the range of lithostatic (250 MPa) to hydrostatic (70 MPa) pressures at which Butte is inferred to have formed (gray shaded field; Tilling, 1973; Roberts, 1975; Dilles et al., 1999; Rusk et al., 2008c).

Application of the Ti-in-quartz thermobarometer of Thomas et al. (2010) to hydrothermal quartz in veins from Butte consistently yields temperatures (Table 2) that are on average 100° to 200°C lower than previous estimates for EDM veins (Roberts, 1973; Brimhall, 1977; Field et al., 2005) and that differ substantially from the other thermobarometry results reported below. As for the magmatic quartz, we conclude that the Ti-in-quartz thermobarometer calibration of Thomas et al. (2010) does not reasonably apply to the natural hydrothermal environment. Alternatively, we have considered the Ti-in-quartz calibration of Huang and Audétat (2012), which not only accounts for the effect of pressure on the solubility of Ti in quartz but also the kinetic effect of variable quartz growth rates, and have evaluated the applicability of this calibration to our data set in more detail.

The abundance of Ti in igneous and hydrothermal quartz (Fig. 8A) varies considerably, as do isobaric temperatures (Fig. 8B) calculated using the calibration of Huang and Audétat (2012). Each column of plotted data displays individual analyses from a single sample. Within each sample type, samples are arranged left to right from deeper to shallower within the deposit and account for fault-corrected elevations for all samples east of the Continental fault (Table 1). Note the presence of generations of quartz that are compositionally distinct from the dominant quartz generation analyzed in each sample. For example, note the distinction between fragments of quartz from the Butte Granite (black triangles) that are suspended within an EDM vein (squares); or QMB vein quartz (diamonds) that is cut by a later formed CL-gray quartz veinlet (dashes); as shown in Figures 3C and 4B, respectively. Concentrations of Ti in each distinct generation of quartz within each sample are remarkably heterogeneous. In the following discussion, we describe characteristics of the dominant quartz generation within a vein unless otherwise noted.

Quartz from the Butte Granite has the highest concentrations of Ti, which ranges from 47 to 157 ppm, among the analyzed samples. CL-bright cores and growth bands in granitic quartz have high Ti concentrations while CL-dark growth bands and interstitial quartz have lower Ti concentrations (Fig. 3A). Corresponding quartz temperatures from the Butte Granite range from ~720° to 900°C. The cooler temperatures from this range are consistent with temperatures we have calculated for granitic biotite, described below, and with water-undersaturated granite cooling near solidus conditions in the upper crust (e.g., 250 MPa). The higher temperatures from this range are consistent with hydrous (2–4 wt % H₂O) granite crystallizing in the upper crust (Holtz and Johannes, 1994; Holtz et al., 2001).

Ti concentrations for quartz phenocrysts from the rhyolitic Steward and Modoc porphyry dikes overlap those of the Butte Granite. The range from low Ti (21 ppm) to high Ti (70 ppm) in porphyritic quartz corresponds to growth bands that oscillate from CL-gray to CL-bright (Fig. 3B). Quartz phenocryst temperatures calculated for these dikes range from 650° to 800°C. Unlike temperatures calculated using the calibration of Thomas et al. (2010), these temperatures are at or above the water-saturated granite solidus at 250 MPa (~650°C), and reasonably correspond to crystallization of hydrous rhyolite with 4 to 7 wt % H₂O (Holtz and Johannes, 1994; Holtz et al., 2001).

One caveat to interpreting any temperature derived from Huang and Audétat (2012) is that the thermobarometer was calibrated using slowly grown quartz (~4–10 μm/day) but growth rates for Butte quartz are unknown. However, Huang and Audétat (2012) successfully demonstrated the applicability of their calibration to quartz grown from eight different igneous systems (including rhyolites and granites), so it is reasonable to assume that quartz growth rates in the Butte Granite and porphyry dikes were comparable and therefore appropriate for use with this thermobarometer. In contrast, we expect the growth rate of hydrothermal quartz to be much more variable. Stockwork veins could include rapidly grown quartz (e.g., quartz grown during rapid decompression from lithostatic to hydrostatic conditions) that incorporated Ti concentrations several times greater than slowly grown quartz at the same temperature (e.g., quartz grown in open fractures at hydrostatic conditions).

Our calculated hydrothermal quartz temperatures are on average only 25° to 75°C higher than previous estimates for EDM and GS veins (Fig. 8B; Roberts, 1973; Brimhall, 1977; Geiger et al., 2002; Field et al., 2005; Rusk et al., 2008c; Reed et al., 2013) and agree moderately well with other thermobarometry results described below. Given our inherent inability to quantitatively estimate vein quartz growth rates, we describe the hydrothermal Ti-in-quartz results in terms of Ti concentrations and speculate on possible temperature implications.

Although Ti dissolution in quartz is complex, especially in hydrothermal quartz, we emphasize that Ti concentrations in vein quartz do vary systematically with CL brightness (e.g., Figs. 3–5), as observed in previous studies (e.g., Müeller et al., 2003; Landtwing and Pettke, 2005; Rusk et al., 2006, 2008a; Mercer, 2009; Müeller et al., 2010). However, many of the quartz generations contain very heterogeneous trace element concentrations, and in practice trace element content is not clearly diagnostic of a particular vein type (e.g., not all BQ is compositionally distinct from EDM or GS quartz; Fig. 8A, Table 2).

Ti concentrations in quartz from hydrothermal veins overlap those of both the Butte Granite and porphyry dike quartz concentrations, ranging from the detection limit (4 ppm) to 102 ppm (Fig. 8A, Table 2). Within each sample, Ti concentrations vary significantly. For example, many hydrothermal vein samples display more variation in Ti concentration (up to 67 ppm Ti) within a single quartz generation than the average difference between samples of the same vein type or between different vein types. These ranges reflect the diversity of CL brightness and textures within each generation of vein quartz (Figs. 4, 5; i.e., excluding variations between distinctly different quartz generations). Ti concentrations in quartz from early-formed, potassically altered biotite crackles, and EDM veins are low, ranging from 4 to 48 ppm. Veins that formed relatively early due to fluid decompression, including the BQ and QMB veins, contain considerably higher concentrations of Ti in quartz, ranging from 8 to 102 ppm. Interestingly, early-formed biotite crackles and EDM veins, which are expected to have relatively high vein formation temperatures (550°–700°C; Roberts, 1973; Brimhall, 1977; Field et al., 2005), have slightly lower Ti concentrations in quartz than do BQ and QMB veins. The more shallow-formed, PGS veins generally have lower

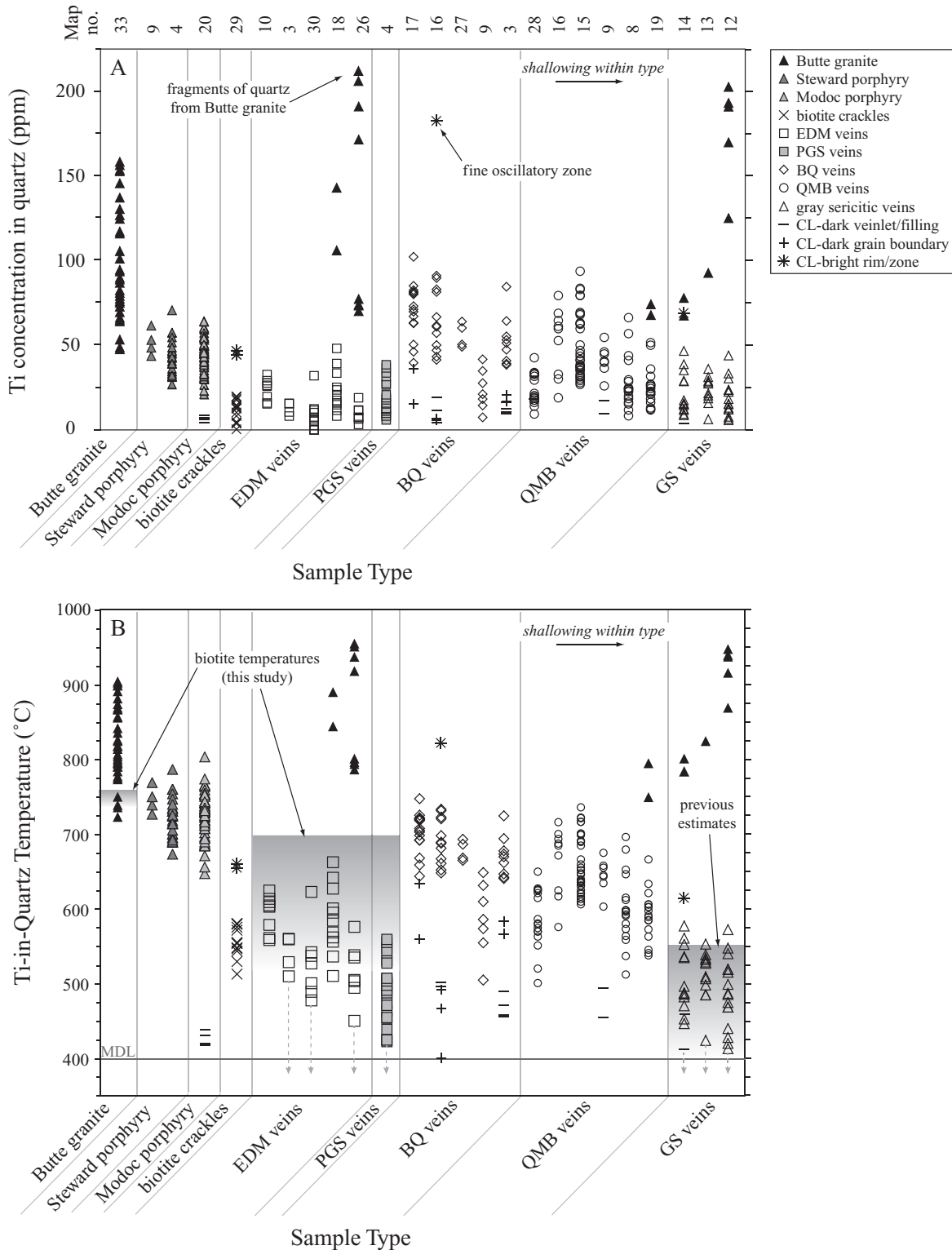


FIG. 8. (A). Ti concentration in igneous and hydrothermal quartz. Each column of data displays multiple analyses from a single sample (see map no.). Note that distinct generations of quartz within each sample are distinguished from the dominant generation of quartz analyzed by unique symbols. See text for more details. (B). Isobaric Ti-in-quartz temperatures calculated using the calibration of Huang and Audétat (2012). Approximate 99% minimum detection limit (MDL) is shown (4 ppm Ti corresponds to ~460°C at 250 MPa and $a_{\text{TiO}_2} = 1.0$; ~400°C at 70 MPa and $a_{\text{TiO}_2} = 1.0$; ~510°C at 250 MPa and $a_{\text{TiO}_2} = 0.5$). For comparison, temperatures we calculate from EDM and PGS biotite are shown in gray shaded field. Previous temperature estimates for EDM veins range from 500° to 700°C (Roberts, 1973; Brimhall, 1977; Field et al., 2005). Previous temperature estimates for GS veins are shown with gray shaded field (Geiger et al., 2002; Rusk et al., 2008c; Reed et al., 2013). Dashed arrows indicate samples containing quartz with Ti concentrations below the detection limit.

maximum Ti concentrations in quartz, ranging from 4 to 38 ppm. The late-formed GS veins, which we expect to have relatively cool vein formation temperatures (400°–550°C; Geiger et al., 2002; Rusk et al., 2008c; Reed et al., 2013), contain low Ti concentrations, ranging from 5 to 46 ppm Ti, as appears reasonable.

One exceptionally high Ti concentration (183 ppm) in BQ corresponds to a finely “oscillatory-zoned” (<10 μm) area (Fig. 5C) and likely represents an intrinsic diffusion-controlled boundary layer effect characterized by nonequilibrium incorporation of Ti (e.g., Shore and Fowler, 1996; D’lemos et al., 1997; Götze et al., 2001), and thus does not accurately represent Ti equilibrium in quartz. Another exceptionally high Ti concentration (70 ppm) in GS quartz corresponds to a CL-bright fracture filling that cuts the main vein (Fig. 4D). Many samples contain well-defined CL-dark veinlets, fracture fillings, and/or grain boundaries, which are difficult to classify as any particular vein type (e.g., classify as EDM, BQ, etc.). These features have Ti concentrations above the detection limit and are distinguished from primary vein quartz (Fig. 8). Ti concentrations in CL-black quartz along thin grain boundaries and filling microcracks (e.g., “spiders and cobwebs”) are consistently below the detection limit (4 ppm), and likely reflect low Ti quartz that formed from post-porphyry, main-tage hydrothermal fluids at cooler temperatures (≤400°C; Rusk and Reed, 2002; Rusk et al., 2008b, c).

Hydrothermal rutile

Neither the Butte Granite nor the porphyry dikes contain primary rutile and thus all of our rutile analyses represent magmatic-hydrothermal transition samples (biotite breccia, biotite crackles) and hydrothermal veins. All of the analyzed samples contain blocky, hydrothermal rutile grains that are subhedral to anhedral, 5 to 800 μm in diameter, and are intergrown with the dominant quartz generation for each vein type, or in the accompanying alteration envelope (Fig. 9). Rutile typically forms grain clusters near hydrothermal biotite and pyrite within veins, and near remnant plutonic biotite in altered wall rock within 1 to 2 mm of veins. Many grains have homogeneous SEM-BSE textures (Fig. 9B) while others preserve faint concentric zoning (Fig. 9C, D), or sector zoning (Fig. 9E). Some grains are irregular (Fig. 9H). Specific textures are not diagnostic of any particular vein type, and examples of each texture are present in single veins. Many rutile grains are intergrown with other hydrothermal minerals such as pyrite, molybdenite, chalcopyrite, and zircon (Fig. 9).

Rutile contains up to several wt % Fe, Nb, and W. Concentrations of Zr and Ta range from 100s to 1,000s of ppm, respectively. Concentrations of all of these elements are heterogeneous within each sample (Table 3). Energy dispersive spectroscopy maps indicate that BSE-bright rutile zones contain more W and Fe than darker rutile zones (Fig. 9E). Zr concentrations do not correlate with Fe or W concentrations, and unlike metamorphic rutile (e.g., Jiao et al., 2010) they are uncorrelated with Ta and only weakly correlated with Nb concentrations.

Zr-in-rutile concentrations measured by microprobe (Fig. 10) vary significantly, as do isobaric temperatures (Fig. 11) calculated using the thermobarometer of Tomkins et al. (2007). The Butte porphyry deposit is estimated to have formed

between lithostatic and hydrostatic pressures of 250 and 70 MPa, respectively (Fig. 10, gray shaded field; e.g., Tilling, 1973; Roberts, 1975; Dilles et al., 1999; Rusk et al., 2008c). The effect of pressure on the Zr-in-rutile thermobarometer is relatively small because the Zr isopleths are steep (Fig. 10). In the case of Butte, the difference between assuming lithostatic or hydrostatic pressure (a difference of 180 MPa) leads to <10°C difference in calculated temperatures. Therefore, we consider the uncertainties associated with pressure assumptions to be negligible, and for the ease of presentation we report our detailed Zr-in-rutile analyses in terms of calculated isobaric temperatures. Following fluid inclusion results of Rusk et al. (2008c) we assume a pressure of 250 MPa for veins that formed near-lithostatic pressure (biotite breccias, biotite crackles, EDM, BQ, and QMB), and 70 MPa for veins that formed near-hydrostatic pressure (PGS and GS).

Calculated Zr-in-rutile temperatures within each sample are heterogeneous (Fig. 11, Table 3), ranging from the minimum detection limit (453°C) to 713°C. For example, many individual samples display more variation in temperature (up to 249°C) than the average temperature difference between samples of the same vein type or between different vein types. Interestingly, the calculated temperature variations qualitatively mimic those determined from Ti-in-quartz concentrations (Fig. 8). The variation in Zr-in-rutile temperatures does not appear to be correlated to any particular textural features observed in BSE images (Fig. 9) or with sample depth within the deposit (Fig. 11). Rutile from magmatic-hydrothermal transitional samples (biotite breccias and crackles) yields temperatures that range from ~473° to 713°C. EDM veins, which are thought to form by combined temperature and pressure drops (Rusk et al., 2008c), show a maximum rutile temperature of 692°C, which is only slightly lower than that for biotite breccias and crackles. Minimum temperatures extend to slightly cooler temperatures (443°C) than biotite breccias and crackles. These temperatures generally agree well with previous estimates (500°–700°C) based on K and Na partitioning in K-feldspar and muscovite (Brimhall, 1977), coexisting ilmenite and hematite pairs (Roberts, 1973), and the distribution of sulfur isotopes in anhydrite-sulfide pairs (Field et al., 2005). Shallower formed PGS veins do not yield such elevated rutile temperatures (up to 646°C), but minimum temperatures (525°C) are considerably higher. BQ veins are most abundant in the deep core of the deposit and evolve upward to QMB, and cut EDM veins. They lack alteration envelopes and are hypothesized to have precipitated dominantly during lithostatic to hydrostatic pressure drops (Rusk and Reed, 2002; Rusk et al., 2008c). Rutile temperatures calculated for BQ and QMB veins range from 444° to 696°C. Late-formed GS veins are prominent in the center of the district, largely above the other vein zones, and cut all other vein types. Until this study, mineral geothermometric data used to constrain GS vein temperatures at Butte were unavailable. It has been assumed that they formed at lower temperatures than the EDM veins because the GS veins formed late, lack K-silicate alteration, and formed at hydrostatic pressure, as indicated by fluid inclusions (Rusk et al., 2008c). B60 fluid inclusions characteristic of GS veins have a maximum estimated trapping temperature of 450°C at a pressure of 70 MPa that is well constrained based on critical homogenization behavior (Rusk

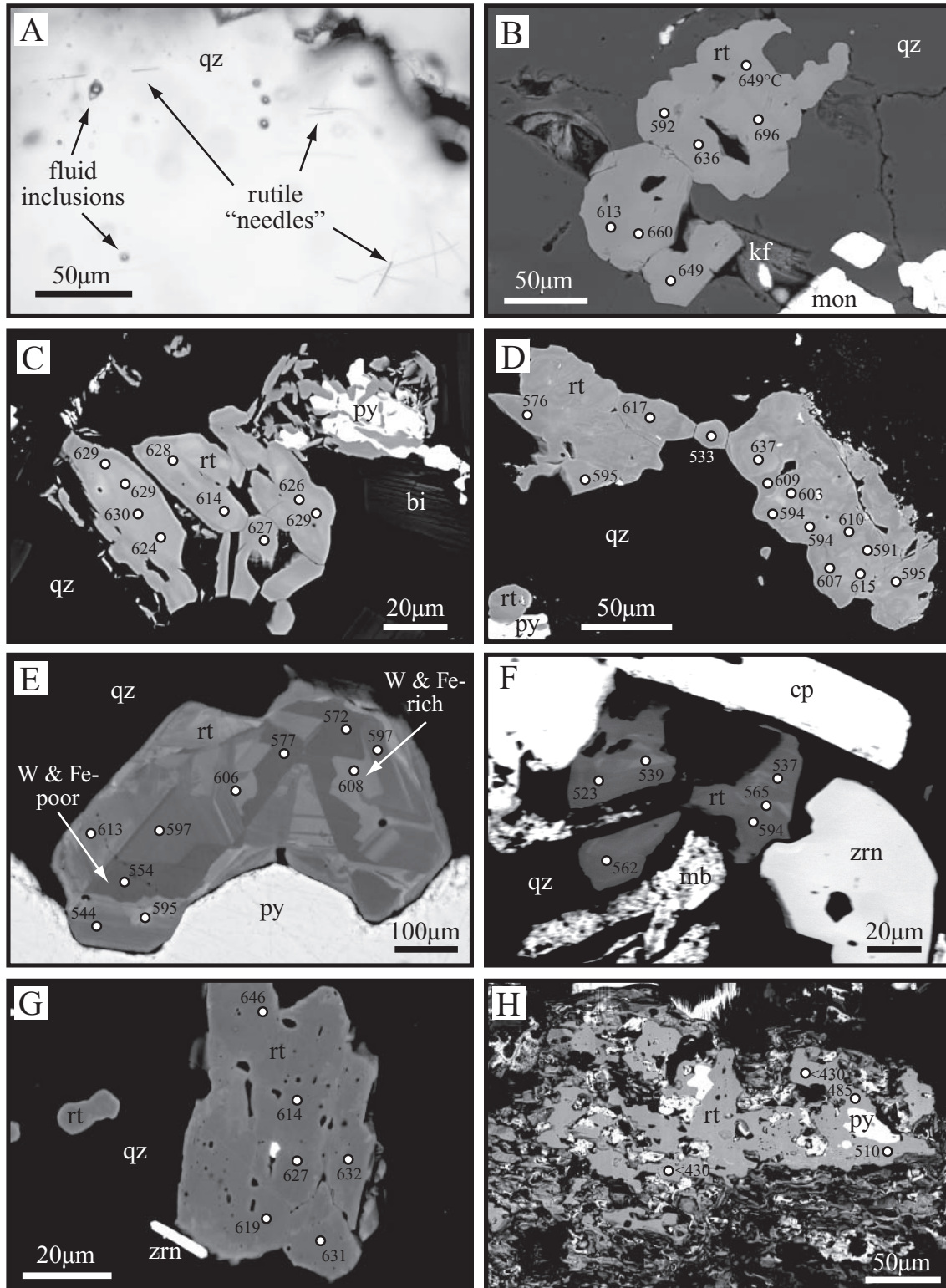


FIG. 9. Representative BSE images of hydrothermal rutile are shown with calculated Zr-in-rutile temperatures ($^{\circ}\text{C}$). (A). Optical photomicrograph of rutile "needles" in quartz (11135-5461); BSE images of blocky rutile with (B) homogeneous texture (11135-5461_rutile5), (C) faint zoning and intergrown pyrite (11135-5051_blockyrutile2), (D) concentric zoning (11135-5051_blockyrutile), (E) sector zoning with Fe- and W-rich bright zones (11135-2470_blockyrutile2), (F) faint zoning with nearby zircon, chalcocopyrite, and molybdenite (11135-3597_rutile), (G) homogeneous texture, inclusions, and euhedral zircon prism (11135-2470_zircon-prism), and (H) irregular texture with intergrown pyrite (10969R-2075_rutile). Abbreviations: bi = biotite, cp = chalcocopyrite, kf = K-feldspar, mb = molybdenite, mon = monazite, py = pyrite, qz = quartz, rt = rutile, zrn = zircon.

TABLE 3. Electron Microprobe Analyses of Trace Elements in Rutile and Calculated Zr-In-Rutile Temperatures

Sample	n	Zr (ppm)	Ta (ppm)	Fe (wt %)	Nb (wt %)	W (wt %)	Zr-in-rutile (°C)
Hydrothermal rutile, in vein							
<u>Biotite breccias</u>							
BU96MR-11_rutile	6	202(38)	977(1561)	2.4(1.8)	0.13(4)	1.2(3)	587(16)
BU96MR-11_rutile2	6	57(14)	245(324)	0.1(1)	0.10(8)	0.10(6)	503(16)
<u>Biotite crackles</u>							
BUR-03-213_rutile2	5	305(28)	153(83)	1.2(9)	0.14(4)	NA	619(7)
BUR98-13_rutile4 ¹	6	504(52)	57	1.0(4)	0.13(3)	1.1(1.2)	659(9)
BUR98-13_rutile3	6	351(18)	77(18)	1.1(2)	0.21(2)	0.78(5)	630(4)
BUR98-13_rutile	6	342(95)	187(218)	1.5(1.1)	0.17(4)	0.7(4)	625(24)
<u>EDM veins</u>							
11185-3771_rutile2	13	85(50)	522(572)	0.4(2)	0.2(2)	NA	518(44)
BUR-03-214_rutile2	12	438(123)	87(22)	1.0(7)	0.27(6)	NA	645(23)
11135-5051_rutile	6	258(23)	56(11)	1.2(8)	0.18(3)	NA	606(7)
11135-5051_blockyrutile	14	242(67)	147(137)	0.9(3)	0.8(4)	NA	598(24)
11135-5051_blockyrutile2	9	336(20)	407(257)	1.2(2)	1.3(1)	NA	626(5)
F2033-488_rutile3 ¹	8	209(185)	498(548)	1.8(8)	0.8(1.4)	2.1(1.5)	571(61)
11135-1150_rutile ¹	1	25	47(18)	1.7(8)	0.05(6)	2.4(1.7)	459
<u>PGS veins</u>							
11135-2470_blockyrutile3 ¹	11	170(51)	103(19)	0.8(3)	0.1(1)	NA	565(22)
11135-2470_blockyrutile2 ¹	10	228(67)	57(10)	1.0(3)	0.12(8)	NA	586(24)
<u>BQ veins</u>							
11185-3771_rutile	9	63(19)	511(523)	0.45(5)	0.15(3)	NA	508(21)
11135-2-4209_rutile	5	245(26)	172(143)	1.1(2)	0.6(2)	1.7(6)	602(8)
11135-2-4209_rutile2 ¹	5	284(44)	211(123)	1.3(3)	1.0(3)	1.2(9)	613(12)
11135-5461_rutile5	7	434(177)	843(585)	1.1(6)	2.3(1.2)	0.31(8)	642(34)
<u>QMB veins</u>							
10969-5699_rutile	9	227(19)	337(250)	0.21(7)	0.6(2)	NA	596(6)
F2033-513_rutile4 ¹	3	43(4)	55(18)	1.6(8)	0.09(2)	3.0(1.9)	488(5)
10969-6804_rutile2	6	123(14)	369(136)	0.42(2)	0.385(8)	0.45(4)	553(8)
10969-6804_rutile3	5	368(8)	1,273(637)	1.10(3)	1.88(3)	0.32(3)	634(2)
11135-3597_rutile2 ¹	6	148(33)	34	1.0(3)	0.06(4)	1.7(9)	565(15)
<u>GS veins</u>							
10969R-2075_rutile	2	58(17)	91(36)	0.3(1)	0.11(4)	NA	498(18)
Hydrothermal rutile, in envelope							
<u>Biotite breccias</u>							
BU96MR-11_rutile3	6	630(166)	742(253)	1.2(3)	0.8(2)	0.6(5)	677(22)
BU96MR-11_rutile4	6	213(96)	243(218)	2.5(1.5)	1.1(6)	1.4(6)	584(42)
<u>Biotite crackles</u>							
BUR-03-213_rutile	9	122(37)	40	0.34(2)	0.042(6)	NA	550(20)
BUR-03-213_rutile3	14	358(44)	91(59)	0.9(2)	0.4(1)	NA	631(10)
BUR98-13_rutile2 ¹	6	475(173)	102(99)	1.1(2)	0.5(1)	1.2(5)	651(28)
<u>EDM veins</u>							
BUR-03-214_rutile	11	190(86)	84(75)	0.7(1)	0.5(2)	NA	573(51)
F2033-488_rutile ¹	10	119(42)	82(35)	1.0(8)	0.2(1)	1.5(1.7)	546(31)
F2033-488_rutile2 ¹	9	90(38)	231(316)	1.6(8)	0.1(1)	2.7(1.7)	528(28)
11135-1150_rutile2	3	44(27)	55(22)	0.71(5)	0.10(5)	0.10(3)	483(37)
11135-1150_rutile3	4	35(10)	59(15)	0.55(4)	0.10(3)	0.013(2)	475(16)
<u>PGS veins</u>							
11135-2470_zircon-prism	6	382(55)	110(43)	0.66(7)	0.58(7)	NA	628(11)
11135-2470_blockyrutile ¹	8	136(41)	248	0.8(4)	0.1(2)	NA	551(19)
11135-2470_blockyrutile4	6	310(52)	220(89)	0.7(1)	0.6(2)	NA	611(13)
<u>BQ veins</u>							
11172-1847_rutile	12	569(90)	1,224(289)	2.2(2)	3.1(4)	NA	669(17)
11172-1847_rutile2 ¹	14	489(232)	261(160)	1.6(6)	1.6(7)	NA	645(57)

TABLE 3. (Cont.)

Sample	n	Zr (ppm)	Ta (ppm)	Fe (wt %)	Nb (wt %)	W (wt %)	Zr-in-rutile (°C)
10969-6804_rutile	5	117(24)	2,371(1374)	0.5(2)	1.4(4)	0.2(1)	549(15)
11135-5461_rutile	4	47(27)	4,051(4063)	0.12(2)	0.11(7)	0.08(1)	487(34)
11135-5461_rutile3	5	270(32)	267(95)	0.68(8)	1.56(3)	0.2(2)	609(9)
QMB veins							
10969-5699_rutile2	7	59(12)	217(134)	0.07(1)	0.23(6)	NA	506(12)
F2033-513_rutile123 ¹	8	61(35)	71(36)	0.6(5)	0.13(8)	1.2(1.8)	501(36)
F2033-513_rutile5 ¹	3	34(5)	39	0.8(5)	0.17(6)	0.9(1.1)	475(9)
11135-3597_rutile ¹	8	129(44)	52(17)	0.9(4)	0.05(4)	1.4(1.2)	554(22)
11135-3597_rutile3	3	77(4)	89(61)	0.76(5)	0.33(4)	0.5(2)	523(3)
11135-2-4209_rutile3	5	328(14)	1,660(1520)	1.2(3)	1.2(1)	0.3(1)	624(3)
11172-4247_rutile	9	413(36)	141(96)	0.73(5)	0.51(9)	0.25(8)	643(7)
11172-4247_rutile2	9	330(43)	114(66)	0.68(8)	0.39(8)	0.2(1)	624(11)
GS veins							
10969-2101_rutile ¹	6	102(12)	114(118)	0.12(6)	0.08(2)	0.2(1)	534(7)
10969-2101_rutile2 ¹	6	74(16)	80(40)	0.2(1)	0.12(4)	0.3(2)	513(13)
10969R-2075_rutile2	13	51(25)	59(34)	0.7(4)	0.17(4)	NA	489(28)
10969-2665_rutile	6	53(27)	68(17)	0.44(3)	0.12(3)	0.5(1)	489(27)
10969-2665_rutile2 ¹	4	43(19)	143(86)	0.9(3)	0.24(7)	1.5(7)	478(24)
10969-2665_rutile3	4	58(4)	332(503)	0.23(2)	0.055(4)	0.58(8)	499(4)
10969-2665_rutile4	3	262(103)	710(561)	0.6(3)	0.37(4)	0.8(7)	596(28)

Notes: Data are reported as averages of multiple microprobe analyses; samples with large standard deviations are highly heterogeneous; numbers in parentheses next to each analysis represents 1σ ; errors given in terms of least unit cited (e.g., 202(38) represents 202 ± 38); n = number of analyses
¹ Denotes sector zoned rutile

et al., 2008c). Thermodynamic fluid modeling (Geiger et al., 2002; Reed and Palandri, 2010; Reed et al., 2013) indicates GS alteration between 400° and 550°C. In addition, muscovite stability suggests a maximum GS vein temperature of ~560°C (Reed et al., 2013) to ~620°C (e.g., Evans, 1965; Montoya and Hemley, 1975). Rutile temperatures calculated for GS veins range from 452° to 628°C, somewhat higher than previous

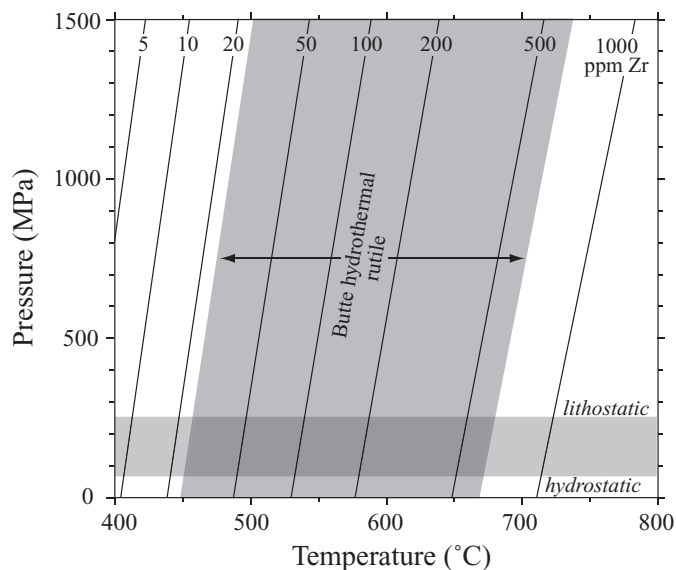


FIG. 10. The range of Zr concentrations in rutile from Butte veins and envelopes is shown (gray shaded field) relative to Zr-in-rutile isopleths (black lines) and corresponding pressures and temperatures from the thermobarometer of Tomkins et al. (2007). Estimated pressures of porphyry formation range from 250 MPa (lithostatic) to 70 MPa (hydrostatic) (gray shaded field; Tilling, 1973; Roberts, 1975; Dilles et al., 1999; Rusk et al., 2008c).

fluid inclusion estimates, but in agreement with thermodynamic modeling and phase equilibrium experiments. The discrepancy between fluid inclusion temperature estimates and those indicated by rutile compositions suggest either (1) that rutile may not have equilibrated in GS veins, or (2) that B60 fluid inclusions may have been trapped after rutile crystallization. Overall, the maximum temperatures from rutile in GS veins are slightly cooler than for all other analyzed vein types, consistent with previous findings.

In 12 samples we analyzed rutile grains in veins and in the accompanying alteration envelope, within 1 to 2 mm of the vein. While only the EDM, PGS, and GS veins have true envelopes, other vein types (e.g., some BQ and QMB veins) have altered selvages that are narrow and show no profound textural changes; consequently these altered selvages are more difficult to identify (e.g., Roberts, 1975). We use a box plot approach (e.g., Tukey, 1977; Tomkins et al., 2007) to represent the range and variability of data for each sample (Fig. 12). In eight of the analyzed sample pairs, temperatures calculated from vein rutile data are indistinguishable from those of alteration envelope rutile (Fig. 12). Three vein samples, one EDM, one BQ, and one QMB have slightly higher vein rutile temperatures, whereas one biotite breccia has higher alteration-envelope rutile temperatures. Samples pairs in Figure 12 show a 40° to 100°C difference between median vein and envelope temperatures. Overall, the temperature range from multiple analyses of rutile from a single vein or alteration envelope is more prominent than the temperature difference between the veins and accompanying alteration envelope.

Igneous and hydrothermal biotite

Primary biotite in the Butte Granite is fresh outside of the Butte district (Fig. 13A) but is recrystallized (“relict”) with a changed composition within the district (Fig. 13B).

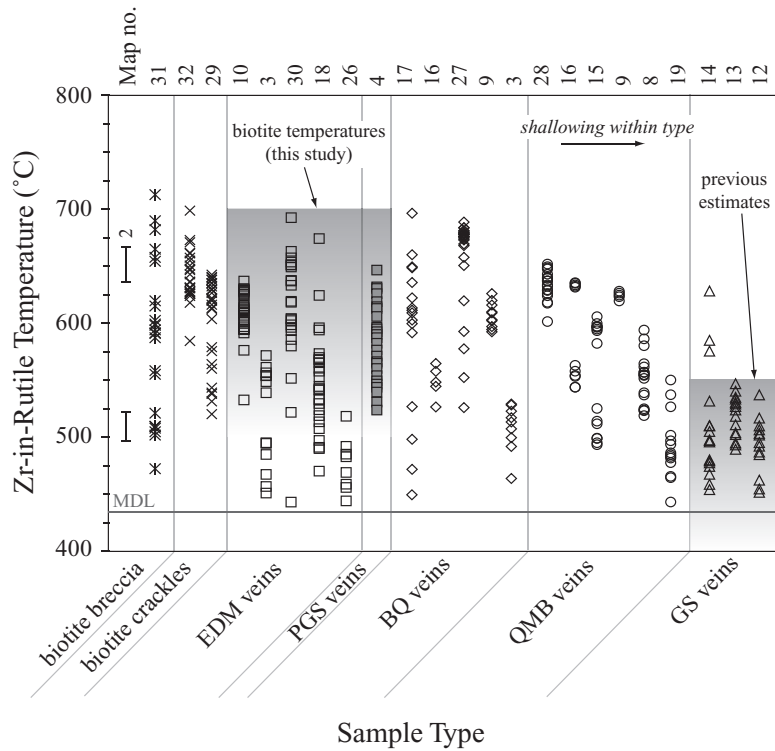


FIG. 11. Isobaric Zr-in-rutile temperatures calculated for all sample types using the thermobarometer of Tomkins et al. (2007). Symbols are the same as in Figure 8. Each column of data displays multiple analyses from a single sample (Table 1, map no.). 2σ temperature precision is shown with bars at left. MDL = 99% minimum detection limit (16 ppm Zr; 436°C at 250 MPa; 430°C at 70 MPa). For comparison, temperatures we calculate from EDM and PGS biotite are shown in gray shaded field. Previous temperature estimates are the same as in Figure 8B (Brimhall, 1973; Roberts, 1973; Geiger et al., 2002; Field et al., 2005; Rusk et al., 2008c; Reed et al., 2013).

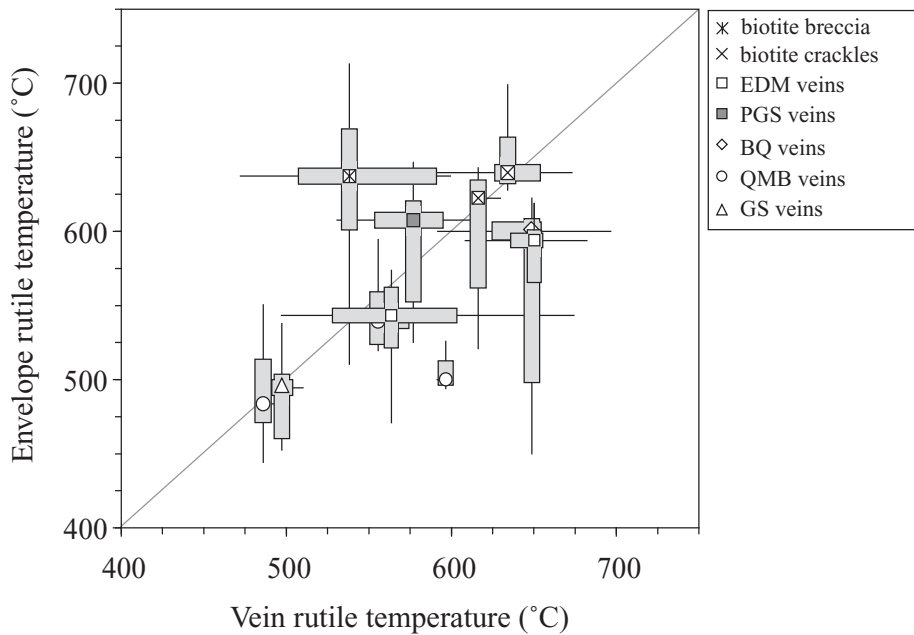


FIG. 12. Zr-in-rutile temperature distributions for rutile in veins and in adjacent alteration envelopes (within 1–2 mm of vein). The range and variability of the data are represented with box plots, where a box of length equal to the interquartile range (representing the most frequent 50% of the distribution) is divided at the median of the data (denoted by unique symbols for each sample type). Each box has “whiskers” that extend to the furthest data point that lies within 1.5 times the interquartile range beyond the edges of the box (representing the tails of the distribution but eliminating outliers that deviate more than $\pm 2.7\sigma$).

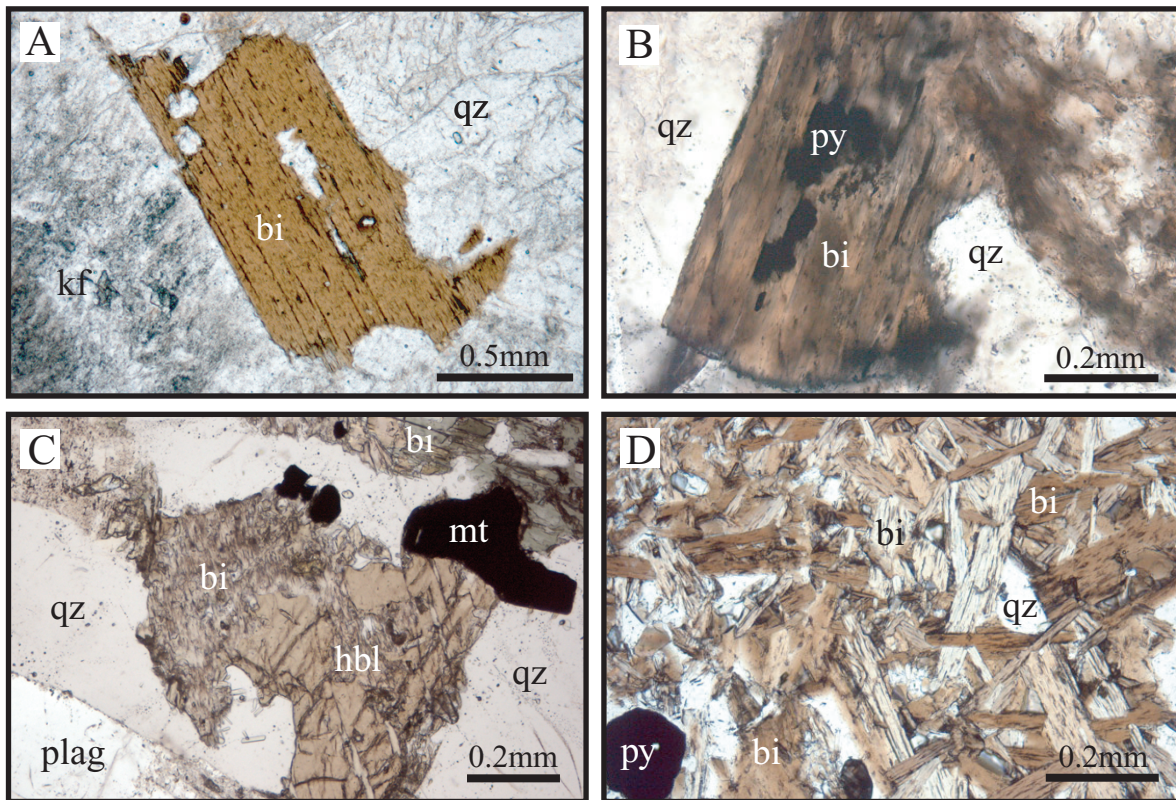


FIG. 13. Optical photomicrographs of biotite types. (A). Fresh Butte Granite biotite (BU-214). (B). Partially altered relict plutonic biotite (10969-2101). (C). Polycrystalline ("shreddy") biotite partially replacing primary hornblende (10969-555.1). (D). Polycrystalline EDM biotite (BUR-03-214). Abbreviations: bi = biotite, hbl = hornblende, kf = K-feldspar, mt = magnetite, plag = plagioclase, py = pyrite, qz = quartz.

Secondary, polycrystalline ("shreddy") hydrothermal biotite occurs in veins and envelopes where it replaces plagioclase and primary hornblende (Fig. 13C, D; Roberts, 1975). All biotite is within the compositional calibration range appropriate to the geothermometer of Henry et al. (2005). Igneous and hydrothermal biotite X_{Mg} (molar $Mg/(Mg + Fe)$) range from 0.50 to 0.85 and TiO_2 contents range from 0.7 to 4.8 wt % (Fig. 14, Table 4; Roberts, 1975; Zhang, 2000). F contents in biotite range from 0.5 to 2.5 wt % and correlate positively with X_{Mg} (Fig. 14B), which is characteristic of other natural and experimentally synthesized biotite (e.g., Munoz and Ludington, 1974; Grew et al., 2006).

Metasomatic alteration proceeds through chemical reactions mediated by a complex mixture of grain boundary diffusion and internal grain diffusion fostered by fluid infiltration along fractures. Consequently, many reactions attain equilibrium only in small volumes (e.g., Thompson, 1970). At Butte, local equilibrium in stockwork veins is likely limited to the vein filling and inner selvage (i.e., millimeters to ~1 cm). Equilibrium also applies on a millimeter scale in the outer selvages, but the outer selvages did not equilibrate with the primary fluid. A disequilibrium-arrested reaction of local pore fluid with host rock is preserved at the outermost transition to fresh rock. In applying the X_{Mg} -Ti-in-biotite geothermometer to natural rocks, Henry et al. (2005) noted that significant disagreements between biotite temperatures and other estimates may indicate alteration, disequilibrium, local equilibrium, or

reequilibration of biotite following peak temperature conditions. Application of this thermometer to rocks from porphyry systems requires evaluation of whether chemical equilibrium was attained and preserved. Below, we evaluate equilibrium for each type of biotite and identify those biotite temperatures that are likely representative of crystallization and recrystallization conditions.

Biotite from five samples of fresh Butte Granite has a pristine texture (Fig. 13A) and uniform chemical composition (Fig. 14A; Roberts, 1975). Ilmenite, which is necessary to buffer TiO_2 chemical potential in the geothermometer, is a ubiquitous accessory mineral adjacent to or as lamellae within magnetite in the Butte Granite. Consequently, temperatures calculated from these biotite compositions (740° – $760^{\circ}C$) reflect equilibrium crystallization during cooling and solidification of granitic magma.

Early-formed EDM veins and PGS veins contain new polycrystalline biotite that lacks sagenitic rutile and small inclusions of Fe-Ti oxides (Fig. 13D). These veins contain ubiquitous subhedral grains of hydrothermal rutile (Fig. 9C; Roberts, 1975), which buffered TiO_2 . Biotite thermometry on these samples indicates crystallization of hydrothermal biotite over a temperature range of 520° to $700^{\circ}C$ (Fig. 14A, Table 4). The large X_{Mg} range for biotite in EDM and PGS/EDM veins is likely due to (1) variable aqueous sulfide activity, which affects Fe availability through variable precipitation of magnetite, pyrite, and chalcopyrite within the adjacent vein

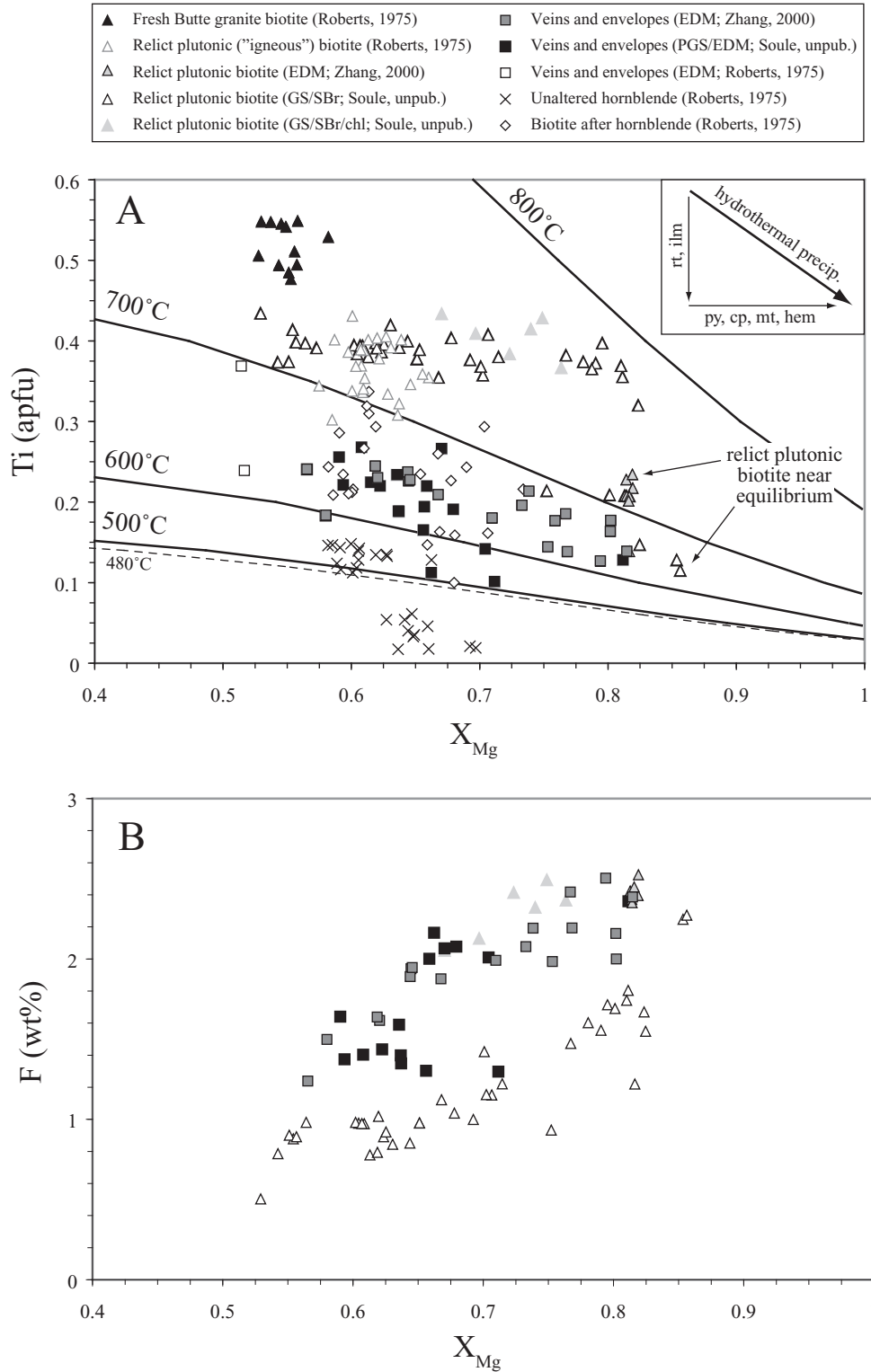


FIG. 14. Compositions of plutonic and hydrothermal biotite. (A). Concentration of Ti (apfu = atoms/formula unit) and Mg mole fraction (X_{Mg} = molar Mg/(Mg + Fe)) in biotite are plotted relative to isotherms from the thermometer of Henry et al. (2005). Errors in calculated temperatures using this geothermometer are smaller than the symbols. Hornblende compositions (calculated based on 23 O) from the Butte Granite are shown for comparison, but the geothermometer does not apply. Inset shows how hydrothermal precipitation of Fe- and Ti-bearing minerals (e.g., cp = chalcopyrite, hem = hematite, ilm = ilmenite, mt = magnetite, py = pyrite, rt = rutile) tends to drive biotite compositions to lower Ti concentrations and higher X_{Mg} . (B). F content in biotite.

TABLE 4. Electron Microprobe Analyses of Biotite, Calculated Formulas (based on 22 O), and Calculated X_{Mg} -Ti-In-Biotite Temperatures

Sample type	PGS/EDM	PGS/EDM	PGS/EDM	GS/SBr	GS/SBr	GS/SBr	GS/SBr	GS/SBr	GS/SBr/chlorite
Biotite texture	Shreddy	Shreddy	Shreddy	Relict	Relict	Relict	Relict	Relict	Relict
Map no.	1	2	6	23	21	25	24	22	11
Sample no.	10772-32a	10778-6	11135-3568	11148-1197	11148-1141	11148-1300	11148-1293	11148-1169.4	10969-1571c
Source	Soule	Soule	Soule	Soule	Soule	Soule	Soule	Soule	Soule
<i>n</i>	4	4	7	8	9	8	7	7	6
Major and minor elements (wt %)									
SiO ₂	31.00(42)	30.73(80)	30.8(2.7)	31.63(19)	31.70(31)	31.48(28)	32.05(25)	32.2(1.0)	31.60(37)
Al ₂ O ₃	24.03(59)	24.5(1.1)	27.1(3.3)	23.26(30)	23.68(85)	22.42(54)	25.6(1.3)	26.9(1.0)	23.84(49)
TiO ₂	1.99(29)	1.72(69)	1.58(42)	3.50(13)	3.49(21)	3.46(13)	3.34(21)	1.75(85)	3.65(22)
FeO ¹	13.26(45)	11.7(1.3)	10.1(1.9)	12.07(88)	11.5(2.1)	14.3(1.1)	6.7(1.4)	6.2(1.2)	9.1(1.1)
MgO	11.90(58)	12.7(1.3)	12.3(1.5)	11.90(48)	12.2(1.0)	10.71(41)	13.9(1.1)	14.9(1.1)	13.40(79)
MnO	0.10(4)	0.12(4)	MDL	0.26(4)	0.19(5)	0.29(5)	MDL	0.27(2)	MDL
K ₂ O	15.99(22)	16.14(23)	16.10(57)	16.09(19)	15.82(44)	16.04(27)	16.21(23)	15.92(29)	15.58(28)
Na ₂ O	0.23(6)	0.33(7)	0.23(4)	0.23(4)	0.22(6)	0.23(4)	0.32(7)	0.18(4)	0.31(3)
CaO	MDL	MDL	MDL	MDL	MDL	MDL	MDL	MDL	MDL
H ₂ O	NA	NA	NA	NA	NA	NA	NA	NA	NA
F	1.40(3)	1.97(23)	1.71(43)	0.88(8)	1.02(21)	0.92(7)	1.64(13)	1.63(50)	2.29(17)
Cl	0.09(2)	0.08(1)	0.06(2)	0.18(4)	0.17(3)	0.19(3)	0.14(3)	0.05(2)	0.15(2)
Total	100	100	100	100	100	100	100	100	100
Formula per 22 O + 4(OH,F,Cl)									
Si	4.645	4.605	4.547	4.696	4.688	4.731	4.655	4.645	4.674
^{iv} Al	3.355	3.395	3.453	3.304	3.312	3.269	3.345	3.355	3.326
Sum iv	8	8	8	8	8	8	8	8	8
Ti	0.224	0.193	0.175	0.391	0.389	0.391	0.365	0.190	0.406
^{vi} Al	0.885	0.933	1.248	0.762	0.810	0.698	1.036	1.216	0.826
Fe	1.661	1.471	1.240	1.499	1.427	1.792	0.813	0.745	1.127
Mg	2.658	2.828	2.703	2.633	2.681	2.400	3.012	3.199	2.956
Mn	0.012	0.015	0	0.032	0.024	0.037	0	0.033	0
Sum vi	5.441	5.441	5.365	5.317	5.331	5.318	5.226	5.382	5.314
K	3.057	3.086	3.028	3.047	2.985	3.074	3.004	2.928	2.940
Na	0.068	0.094	0.067	0.065	0.063	0.067	0.091	0.050	0.088
Ca	0	0	0	0	0	0	0	0	0
Sum xii	3.124	3.181	3.095	3.112	3.049	3.142	3.096	2.979	3.029
Sum cations	16.565	16.621	16.460	16.430	16.380	16.459	16.322	16.361	16.343
X_{Mg}^2	0.62(2)	0.66(5)	0.68(6)	0.64(3)	0.65(6)	0.57(3)	0.79(4)	0.81(4)	0.72(3)
Temperature (°C)	642(21)	617(74)	620(46)	n/a	n/a	n/a	n/a	n/a	n/a

Notes: Numbers in parentheses next to each analysis represent 1σ on average of multiple analyses; errors given in terms of least unit cited (e.g., 31.00(42) represents 31.00 ± 0.42); *n* = number of analyses, NA = not analyzed, MDL = below the 99% minimum detection limit, n/a = not applicable

¹ All Fe reported as FeO[°]

² X_{Mg} = molar[Mg/(Mg + Fe)]

and envelope (Fig. 14A, inset), and (2) incorporation of different amounts of F (Fig. 14B; e.g., Munoz and Ludington, 1974; Grew et al., 2006).

Hydrothermal recrystallization of plutonic biotite was rarely complete and appears to have been out of chemical equilibrium with metasomatizing fluids (Roberts, 1975). Most relict biotite grains contain ~1% small Fe-Ti oxide inclusions and sagenitic rutile due to cooling and exsolution from high-temperature Ti-rich biotite (Roberts, 1975). The indicated temperatures, between 680° and 740°C (Fig. 14A), are not representative of hydrothermal processes, but rather indicate an incomplete compositional transition between primary granite biotite (740°–760°C) and early dark biotite that precipitated from early hydrothermal fluids (520°–700°C).

Relict plutonic biotite adjacent to GS alteration envelopes (Fig. 13B) was rarely completely recrystallized, contains sagenitic rutile, and also appears to have been out of chemical equilibrium with the metasomatizing fluid despite

hydrothermal rutile in these veins that should have buffered the activity of TiO₂. Derived temperatures range from 700° to 790°C (Fig. 14A) and are significantly hotter than those previously estimated for this type of late alteration (400°–550°C; Geiger et al., 2002; Rusk et al., 2008c; Reed et al., 2013) and our calculated rutile temperatures (~450°–630°C). Estimates of muscovite stability temperatures ($\leq 620^\circ\text{C}$; Evans, 1965; Montoya and Hemley, 1975; Reed et al., 2013) also suggest that these biotite temperatures do not represent prevailing conditions during GS alteration. Relict biotite compositions extend to higher X_{Mg} than those of relict biotite adjacent to EDM alteration, which likely reflects Fe removal from biotite into abundant pyrite that formed in adjacent intense sericitically altered rock.

Hydrothermal biotite that replaced primary hornblende is compositionally variable even within single pseudomorphed hornblende grains. These grains do not contain Fe-Ti oxides (Roberts, 1975) and thus the compositional variability is not

a reflection of composite microprobe analyses. Instead, Roberts (1975) suggested that biotite that replaced hornblende reached equilibrium only on a local scale, and their compositional heterogeneity may have been inherited from the original amphibole (Fig. 14A), which is composed of two species, actinolite and hornblende, within single grains. Thus, as determined for relict plutonic biotite, calculated temperatures of 500° to 715°C for biotite that replaced hornblende do not indicate hydrothermal alteration conditions.

Compositions of two relict plutonic biotite samples coincide with somewhat reasonable isotherms and may indicate formation under conditions that approached equilibrium (Fig. 14A). Specifically, six biotite analyses from one GS sample (11148–1169.4) are consistent with temperatures that range from 650° to 710°C, and one indicates 770°C. This sample may suggest that this particular biotite formed under near-equilibrium conditions with GS fluids, perhaps due to a high fluid/biotite ratio. However these temperatures are still higher than likely prevailed for GS alteration.

Discussion

Comparison of Zr-in-rutile and Ti-in-quartz thermobarometers

Isobaric temperature distributions calculated for magmatic-hydrothermal transitional samples (biotite crackles) and hydrothermal veins using Zr-in-rutile (Tomkins et al., 2007) and Ti-in-quartz (Thomas et al., 2010; Huang and Audétat, 2012) help to define the conditions that prevailed during mineralization processes in the Butte district (Fig. 15). The Ti-in-quartz calibration of Thomas et al. (2010) produces median temperatures for hydrothermal veins that are 50° to 200°C lower than Zr-in-rutile temperatures, and temperatures for quartz from EDM veins are substantially lower (170°–350°C lower) than

several previous independent estimates (Roberts, 1973; Brimhall, 1977; Geiger et al., 2002; Field et al., 2005; Rusk et al., 2008c; Reed et al., 2013). The Thomas et al. (2010) calibration is evidently inappropriate when applied to natural igneous quartz, because despite allowing for possible errors in the a_{TiO_2} and pressure used for calculations (e.g., Thomas and Watson, 2012), it returns unreasonable subsolidus temperatures for quartz phenocrysts from the rhyolitic Butte porphyry dikes (Fig. 7) and similarly unreasonable results for the Oruanui and Bishop Tuff rhyolites (Wilson et al., 2012). These results suggest fundamental problems with the Thomas et al. (2010) calibration and/or nonequilibrium Ti concentrations in Butte quartz.

In their study of Ti-in-quartz, Huang and Audétat (2012) found that kinetic factors also affect the concentration of Ti-in-quartz. Their experiments show that when quartz grows more slowly (4–10 $\mu\text{m}/\text{day}$), it equilibrates with rutile and incorporates less Ti into its crystal structure, and thus taking growth rate into account provides more accurate thermobarometric results. This Ti-in-quartz calibration yields median temperatures for Butte veins that are within 80°C of Zr-in-rutile temperatures (Fig. 15), which agrees quite well within the wide range of temperatures that exists for each vein type, both from quartz and rutile. It also reproduces hydrothermal vein temperatures that have been independently determined for EDM and GS veins (Fig. 8B; biotite in this study; Roberts, 1973; Brimhall, 1977; Geiger et al., 2002; Field et al., 2005; Rusk et al., 2008c; Reed et al., 2013). Agreement between Ti-in-quartz and Zr-in-rutile temperature estimates suggests that at least some of the hydrothermal quartz at Butte grew slowly enough to incorporate near-equilibrium Ti contents. The thermobarometer of Huang and Audétat (2012) produces reasonable temperatures for granitic and rhyolitic quartz from Butte (Fig. 8B) and eight other igneous systems. We therefore consider

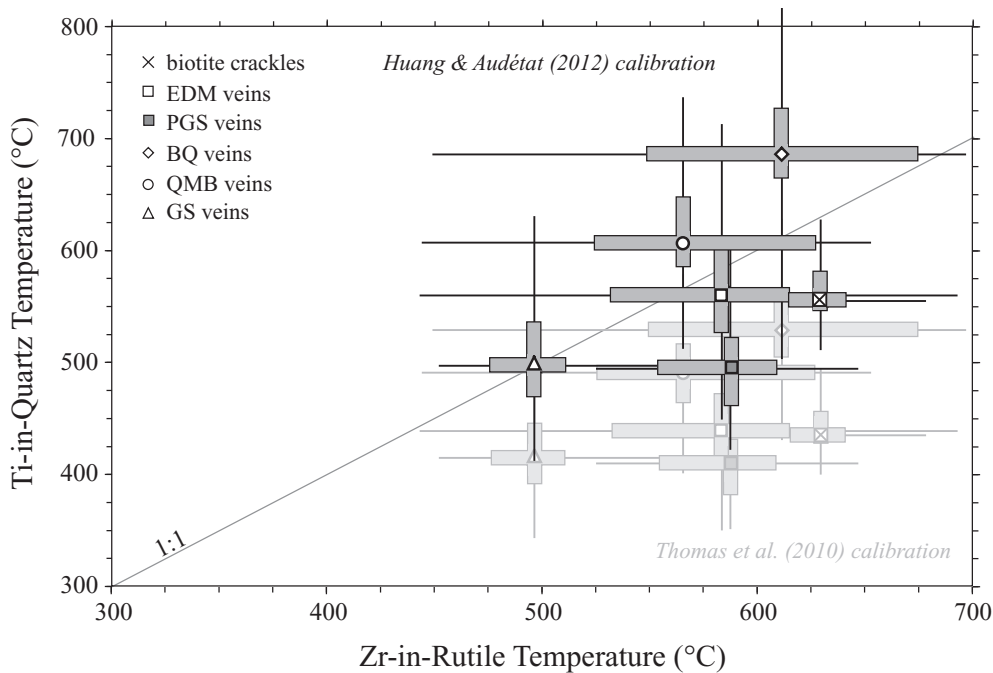


FIG. 15. Box plots for isobaric Ti-in-quartz and Zr-in-rutile temperatures for transitional and hydrothermal samples (see text for further details).

the temperatures derived from this version of the Ti-in-quartz thermobarometer to be more accurate than those produced by the Ti-in-quartz thermobarometer of Thomas et al. (2010).

Wide range in mineral compositions

Distinct generations of igneous and hydrothermal quartz, rutile, and biotite consistently display large ranges in trace element concentrations. Of particular interest are the ranges of trace element abundances pertinent to the quartz, rutile, and biotite thermobarometers and implicit broad temperature ranges (Tables 2–4; Figs. 8, 11, 14). Data from other studies of the Butte porphyry Cu deposit also imply development within a highly variable thermal regime. For example, estimates of the temperatures that prevailed during EDM and PGS vein formation based on the distribution of sulfur isotopes from anhydrite-sulfide pairs range over $\sim 150^\circ\text{C}$ for cocrystallized minerals (Field et al., 2005). Fluid inclusion homogenization temperature distributions range over 100° to 200°C for individual fluid inclusion assemblages (i.e., assemblages distinguished by average bubble vol %: B35, B60, B85, and B20; Rusk et al., 2008c), which translates to a widespread in calculated isochors for a particular fluid inclusion population. This range in isochors implies that the fluids experienced significant changes in either temperature and/or pressure during ascent and trapping; although these variations could be interpreted as indicating significant postentrapment inclusion modifications (e.g., necking or leaking). Rusk et al. (2008c) reported petrographic evidence for significant postentrapment modifications only for B15H and B35 inclusions from samples overprinted by later pyrite veins, but they avoided such inclusions during their analyses.

Butte is not the only porphyry Cu deposit for which these large trace element concentrations have been documented. For example, Ti-in-quartz thermometry for the Central Oyu Tolgoi and Zesen Uul porphyry Cu deposits in Mongolia reveals early BQ stockwork vein formation over a broad range of temperatures, from $\sim 600^\circ$ to 880°C (Müller et al., 2010). Although the absolute temperatures reported by Müller et al. (2010) for these deposits are probably inaccurate since they used the original 10 kbars calibration of the Ti-in-quartz thermometer (Wark and Watson, 2006), their data represent a large range in Ti concentrations within a single generation of quartz formation. Similarly, Zr-in-rutile thermometry for the dacite porphyry of the El Teniente porphyry Cu-Mo deposit in Chile also suggests vein formation over a large temperature range (470° – 680°C), which Rabbia et al. (2009) interpreted as representing superimposed episodes of potassic and phyllic alteration, each of which developed over a $\sim 100^\circ\text{C}$ range. Typically, highly variable data derived from mineral and fluid inclusion thermobarometry are averaged for simplicity, but such data processing may obscure critical details pertinent to fundamental natural processes responsible for porphyry Cu deposit formation.

Effects of physicochemical variations: Pressure, temperature, activity of TiO_2 (or SiO_2), and crystal growth rate variations may contribute to the range in Ti and Zr concentrations typical of quartz and rutile, respectively, from the Butte district. For the biotite thermobarometer, identifying factors potentially responsible for the range of biotite compositions is challenging because the biotite thermobarometer is

empirically based. Accepting the empirical calibration as is, the observed range in equilibrated biotite compositions corresponds to a 20°C spread in formation temperatures for granitic biotite and nearly 200°C for hydrothermal biotite (Fig. 14).

Zr-in-rutile thermobarometer results for Butte samples are relatively straightforward to interpret, because hydrothermal rutile grew in the presence of zircon and quartz, the activity of SiO_2 is fixed by quartz, and crystal growth rate is not known to be an important factor. The Zr-in-rutile thermobarometer is particularly robust because pressure variation has a relatively small effect on partitioning Zr into rutile (Fig. 10).

In contrast, interpreting the results from the Ti-in-quartz thermobarometer, particularly for hydrothermal quartz, is more challenging. For granitic quartz, temperature interpretations are relatively straightforward. Pressure changes during quartz crystallization were likely to be limited as the Butte Granite evolved and solidified within the crust, and interstitial quartz likely grew essentially isobarically. Although the true value for a_{TiO_2} in the system may differ from the assumed value, variation of a_{TiO_2} during granite solidification was likely insignificant because changes in temperature and composition are expected to have been relatively small, thereby limiting the range of TiO_2 solubility (Hayden and Watson, 2007). Finally, the quartz growth rate that dominated as the granite cooled and solidified was likely relatively slow and continuous. Thus, the 720° to 900°C temperature range we observe for the Butte Granite (Fig. 8B) most likely reflects the prevailing thermal range during granite solidification.

Quartz phenocrysts from the Butte porphyry dikes likely experienced more dynamic physicochemical conditions during their growth than quartz from the Butte Granite. Pressures may have changed, perhaps by ~ 50 to 100 MPa if the hydrous magma within the cupola was brought up from several kilometers below. The activity of TiO_2 may have varied temporally if the cupola experienced periodic injections of new magma with a different a_{TiO_2} . In addition, crystal growth rate may have varied as a function of other fluctuating conditions (e.g., changes in pressure or water content). Thus the isobaric temperature range recorded by porphyry quartz phenocrysts (650° – 800°C ; Fig. 8B) could be compressed (or expanded), perhaps by as much as $\sim 30^\circ$ to 60°C , by allowing for variability in pressure, a_{TiO_2} , and quartz growth rate (e.g., ± 100 MPa, $\pm 0.2 a_{\text{TiO}_2}$, $\pm 10 \mu\text{m}/\text{day}$).

Relative to igneous quartz, stockwork quartz veins likely experienced the most dynamic crystallization conditions. Fortunately, the presence of rutile in all of our hydrothermal samples fixes a_{TiO_2} to 1.0 and thus removes a_{TiO_2} as a variable. Butte fluid inclusion isochors combined with independent estimates of vein temperatures indicate that lithostatic to hydrostatic pressures prevailed during quartz deposition by vein-forming fluids (Rusk et al., 2008c). These fluid inclusion data constrain how much pressure variations affect calculated isobaric temperature ranges for hydrothermal quartz (Fig. 8B). Fluid inclusions from deep BQ, QMB, and EDM veins, for which we assumed an isobaric pressure of 250 MPa, indicate pressure variations from 150 to 270 MPa, which could lead to errors in calculated isobaric temperatures of $+5^\circ$ to -35°C . For more shallowly formed veins, we assumed an isobaric pressure of 70 MPa. Fluid inclusions from PGS veins

indicate pressures varying from 40 to 110 MPa, corresponding to potential errors of $\pm 35^\circ\text{C}$ in calculated isobaric temperatures, while those from late-formed GS veins indicate pressures that range from 30 to 70 MPa, resulting in isobaric temperatures that could be up to $\sim 25^\circ\text{C}$ too high for the lowest pressure.

A drop in pressure can effectively initiate quartz precipitation from hydrothermal fluids (Rusk and Reed, 2002) and can also produce a large range in hydrothermal quartz growth rates. On average, we expect the most slowly grown hydrothermal quartz in the Butte pre-Main stage to be from GS veins. Quartz in these veins probably grew at 0.5 to 5 $\mu\text{m}/\text{day}$, based on an average vein width of 1 to 2 cm and reactive transport modeling estimates of 10 to 100 years required for alteration envelope formation (Geiger et al., 2002). These growth rates are within the range of those Huang and Audétat (2012) used to calibrate the Ti-in-quartz thermobarometer. GS veins experienced the smallest variation in pressure, grew relatively slowly, and contain the most abundant euhedral crystal forms. Therefore, of all the vein types analyzed, the range of Ti concentrations in quartz from GS veins most closely illustrates the thermal variability of the stockwork veins, with minimal effects from pressure and growth rate variations. Significantly, the median Ti-in-quartz temperatures from GS veins agree perfectly with their Zr-in-rutile temperatures (Fig. 15).

In contrast, BQ and QMB veins, which lack readily visible alteration envelopes, probably formed relatively quickly during hydrofracturing events in response to rapid decompression from lithostatic to hydrostatic conditions (Rusk and Reed, 2002; Rusk et al., 2008c). Consequently, the range of Ti concentrations in quartz could reflect a substantial effect from pressure in addition to temperature. Quartz from these veins may also have formed at much faster rates than GS quartz, perhaps even several orders of magnitude faster, which may have fostered higher, nonequilibrium Ti contents. Ti-in-quartz temperatures from these veins are higher on average than those calculated from rutile (Fig. 15), as expected if quickly grown quartz incorporates proportionately higher Ti concentrations.

Fluid inclusion data (Rusk et al., 2008c) suggest that EDM veins and PGS veins formed between lithostatic and hydrostatic pressures and had sufficient time to develop alteration envelopes. Biotite crackles also formed between lithostatic and hydrostatic pressures, but their narrow envelopes ($< 1\text{ mm}$) indicate a short duration of wall-rock reaction. Although the quartz growth rate for these potassic veins is unknown, it is likely intermediate between that of GS veins and BQ or QMB veins. Ti concentrations in quartz from potassic veins yield temperatures $\sim 50^\circ\text{C}$ lower on average than those for rutile (Figs. 8, 11). The cause of low Ti in quartz from early-formed, biotite crackles and EDM veins, where we expect high temperatures and high Ti concentrations, is unclear but may relate to preferential loss of Ti during expulsion of fluid from quartz upon transitioning from beta to alpha quartz (Barker and Robinson, 1984; Griffen, 1992). The beta-alpha transition occurs at $\sim 600^\circ\text{C}$ at the lithostatic pressures applicable to Butte. Therefore, the EDM veins would have experienced this transition, but so too should the BQ and QMB veins.

Although the ranges of Ti concentrations in hydrothermal quartz can be partially explained by variations in pressure and

quartz growth rate, as discussed above, they must also largely reflect variations in formation temperature. Within a single generation of quartz (as distinguished by CL), Ti-in-quartz temperatures vary by as much as 150° to 200°C (Figs. 8B, 15). However, deviations from lithostatic to hydrostatic pressures can only account for up to $\sim 70^\circ\text{C}$ of this range and an order of magnitude change in quartz growth rates only accounts for $\sim 80^\circ\text{C}$. Also of significance, quartz from GS veins, which grew relatively slowly and in a relatively uniform pressure regime, is consistent with a temperature range ($\sim 130^\circ$ – 200°C) as broad as any other vein type.

Attainment of chemical equilibrium: Failure to achieve chemical equilibrium with the buffering assemblage (i.e., rutile, quartz, and zircon) on the timescales pertinent to vein and envelope formation may also have contributed to the highly variable ranges observed for Ti and Zr concentrations in quartz and rutile. For example, quartz may have grown so fast that it incorporated excess Ti (as discussed above; Huang and Audétat, 2012) or perhaps rutile grains were too far away to effectively buffer Ti in quartz. Analyzed relict biotite grains contain anomalously high Ti concentrations (Fig. 14) that confirm the occurrence of disequilibrium conditions, underscoring the need to consider whether disequilibrium processes affected quartz and rutile compositions. We observed that unaltered primary biotite in the Butte Granite achieved and preserved textural and geochemical equilibrium, as did freshly grown hydrothermal biotite (Fig. 14). Similarly, in the presence of the appropriate mineral buffers original igneous and freshly grown hydrothermal quartz and hydrothermal rutile should have achieved equilibrium compositions more readily than relict, metasomatized quartz and rutile. As for all mineral thermobarometers, establishing petrographically that components of a particular buffering mineral assemblage grew simultaneously and proving equilibrium is a significant challenge. However, we have documented systematic patterns of trace element distributions in quartz and rutile. Most notably is the correlation between Ti concentrations in quartz with crystal textures observed in SEM-CL (Figs. 3–5) and the manner in which concentration ranges in Zr in rutile qualitatively mimic those of Ti in quartz (Figs. 8, 11). These observations, and especially broad agreement among the thermobarometers (Fig. 15) and with previous independent estimates, lead us to conclude that local equilibrium was essentially achieved with the appropriate buffering assemblage during precipitation of quartz, rutile, and hydrothermal biotite.

Postcrystallization diffusion of trace elements: Although equilibrium trace element concentrations were probably achieved during the formation of quartz and rutile, these equilibrium concentrations may have been affected by postcrystallization diffusion of trace elements. Diffusion rates for Ti in quartz and Zr in rutile are both exceedingly slow (Cherniak et al., 2007a, b) relative to the 1- to 2-m.y. time required to form the Butte deposit (Lund et al., 2002; Dilles et al., 2003). For example, Ti can diffuse $\sim 15\ \mu\text{m}$ at 600°C in quartz over 1 m.y. and Zr diffusion in rutile is ~ 4 times slower (Cherniak et al., 2007a). We observe that different generations of igneous and hydrothermal quartz maintained their original, distinct petrographic and geochemical characteristics. For example, quartz Ti concentrations correlate directly with SEM-CL features, such as growth zones, crosscut veinlets, and fragments

of Butte Granite quartz suspended in vein quartz owing to the slow diffusion of Ti in quartz (Figs. 3–5). Although we have not observed analogous SEM-BSE textural and chemical correlations in rutile, it is likely that initial concentrations of Zr in hydrothermal rutile were preserved even better than those of Ti in quartz because Zr diffusion in rutile is slower than Ti diffusion in quartz. Thus postcrystallization diffusion of elements cannot account for the range in trace element concentrations that we have measured. Furthermore, postcrystallization diffusion would be expected to homogenize original concentrations, thereby decreasing the ranges. Therefore our analytical Ti and Zr concentrations largely represent the original concentrations formed during quartz and rutile crystallization.

Rabbia et al. (2009) suggested that the large range of Zr-in-rutile temperatures characteristic of the El Teniente porphyry Cu-Mo deposit result from resetting by superimposed episodes of potassic and phyllic alteration. However, resetting Zr requires diffusion after initial crystallization, but as indicated above, diffusion rates are exceedingly slow. Consequently, resetting by superimposed hydrothermal episodes seems implausible.

Distinguishing different mineral generations: The diversity of Ti and Zr concentrations may also reflect mistakenly combining data from unique generations of quartz and rutile. However, textures observed in SEM-CL and BSE images do not support further subdivision. Many of the broad ranges in trace element concentrations represent variations across remarkably small, millimeter-scale veinlets with small grain sizes (Figs. 3–5, 9). For example, the concentration of Zr in a single cluster of rutile 150 μm wide in one BQ vein (Fig. 9B) ranges from 214 to 764 ppm (i.e., 592°–696°C). In addition, biotite crackles, whose textures demonstrate they are monogenetic, show as wide a range in Zr concentrations in rutile (and temperatures) as any other sample type (Fig. 11). Regardless of whether we can accurately distinguish from one another the textures tied to distinct trace element concentrations within single veinlets, the occurrence of large compositional ranges over small spatial scales points to a dynamic physicochemical genesis.

We conclude that quartz, rutile, and nonrelict biotite retain their original Ti, Zr, and $X_{\text{Mg-Ti}}$ distributions, respectively. If disequilibrium prevailed, then correlations of temperature and concentrations discussed above are serendipitous. If equilibrium prevailed, then the compositional trends we observe provide meaningful clues to the thermal processes of magmatic-hydrothermal deposit formation. Consideration of the Zr-in-rutile and Ti-in-quartz thermobarometry, along with the $X_{\text{Mg-Ti}}$ -in-biotite thermobarometer provides a new view on the space-time evolution of the deposit's thermal profile.

Butte deposit thermal profile

Starting with the early Butte maps by Meyer et al. (1968) where the deposit-scale shape of the distribution of Butte QMB veins was described as “the moly dome,” the distribution of Butte alteration and vein zones, mapped as metasomatic isograds (Reed et al., 2013), define domical shapes around the mineralization centers (e.g., the magnetite zones, Fig. 2). Although the dome forms are accurate as isograds showing the distribution of alteration and vein minerals, our thermometry suggests that the isograds do not portray the temperature distribution at any given time; that is, in contrast to the use of

isograds in the context of regional metamorphism, we should not regard metasomatic isograds at Butte as isotherms.

Given the reevaluation of the Ti-in-quartz thermobarometer (Thomas and Watson, 2012; Wilson et al., 2012), and the complications associated with interpreting temperatures in the absence of quartz growth rate information (Huang and Audétat, 2012), our conclusions concerning the thermal evolution of the Butte Granite and porphyry quartz phenocrysts is limited to the systematic variations in SEM-CL textures and corresponding Ti concentrations in quartz. Ti-in-quartz temperatures for the Butte Granite span a large range (720°–900°C) that likely captures temperatures experienced throughout the solidification of the granitic magma reservoir (Fig. 16). The highest temperatures (800°–900°C) are from quartz with alternating CL-bright to CL-gray growth bands that resemble phenocryst zonation (Fig. 3A) and probably reflect early crystallization when the water-undersaturated magma retained a moderate melt fraction. The lowest temperatures (720°–800°C) are from CL-gray interstitial quartz that must have crystallized during later stages of magma solidification. Unaltered biotite from the Butte Granite preserves a restricted range of granite temperatures (740°–760°C) that overlap with late-stage quartz temperatures (Fig. 16). Given that Ti, Mg, and Fe are apparently highly mobile in biotite (Fig. 14A; Henry et al., 2005), we suggest that these temperatures represent conditions prevailing near the end of the granite cooling history.

Quartz porphyry dikes that intruded the Butte Granite are ~10 m.y. younger than their host and reflect a separate magmatic event (Lund et al., 2002). Porphyry Cu deposits are generally accepted to form directly from fluids exsolved from porphyritic magma (e.g., Seedorff et al., 2005; Sillitoe, 2010). Our data are consistent with some early exsolved fluids having been at magmatic temperatures, which could extend as low as ~650°C near the 250 MPa water-saturated granite solidus (Fig. 16; e.g., Naney, 1983; Dall'Agnol et al., 1999; Holtz et al., 2001; Klimm et al., 2003) and would commonly have been as high as ~700°C, given the high H₂O contents (>5–6 wt %) and low crystallinity (~25%) determined for the Butte porphyry dikes (Mercer, 2009). Application of the Ti-in-quartz thermobarometer to phenocrysts from Butte porphyry dikes suggests magmatic temperatures that ranged from 650° to 800°C (Fig. 16), in agreement with our hypothesized temperature range, but extending it to considerably higher temperatures. The coolest temperatures are from CL-gray phenocryst cores (possibly xenocrysts) and from alternating CL-gray rims, while the highest temperatures are from CL-bright rims (e.g., Fig. 3B).

Ti-in-quartz and Zr-in-rutile temperatures from magmatic-hydrothermal transition samples and stockwork veins range from ~410° to 750°C. The high end of this range overlaps with estimated magmatic temperatures from porphyry dikes (650°–800°C) as expected since these features emanate directly from the dikes. These results demonstrate that there is a thermal continuum between magmatic and hydrothermal realms in the Butte system (Fig. 16).

Similar to biotite breccias and crackles, all hydrothermal vein samples exhibit a substantial overlapping range of temperatures (Fig. 11). We interpret the highest temperatures from early, deep hydrothermal veins (~700°C; Fig. 11) to

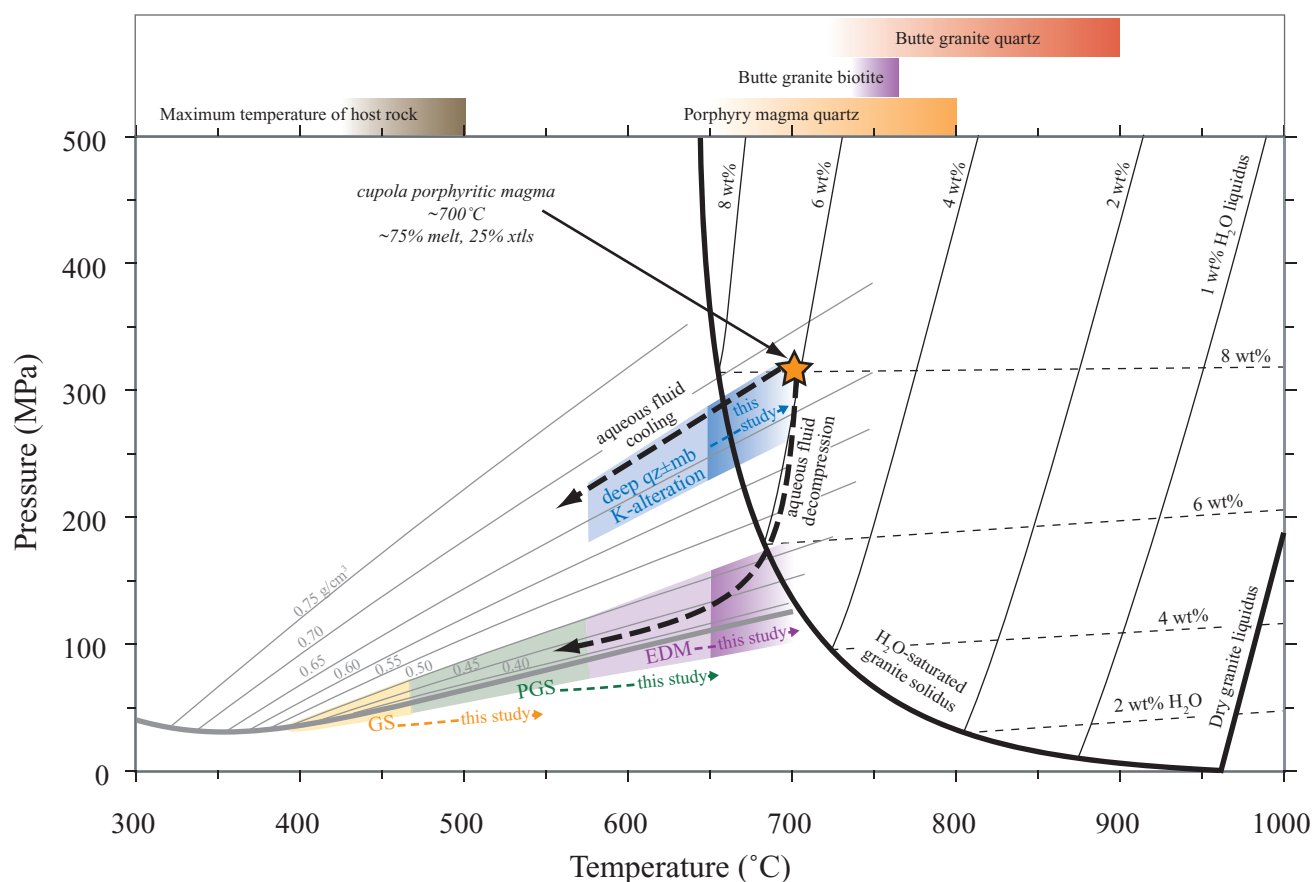


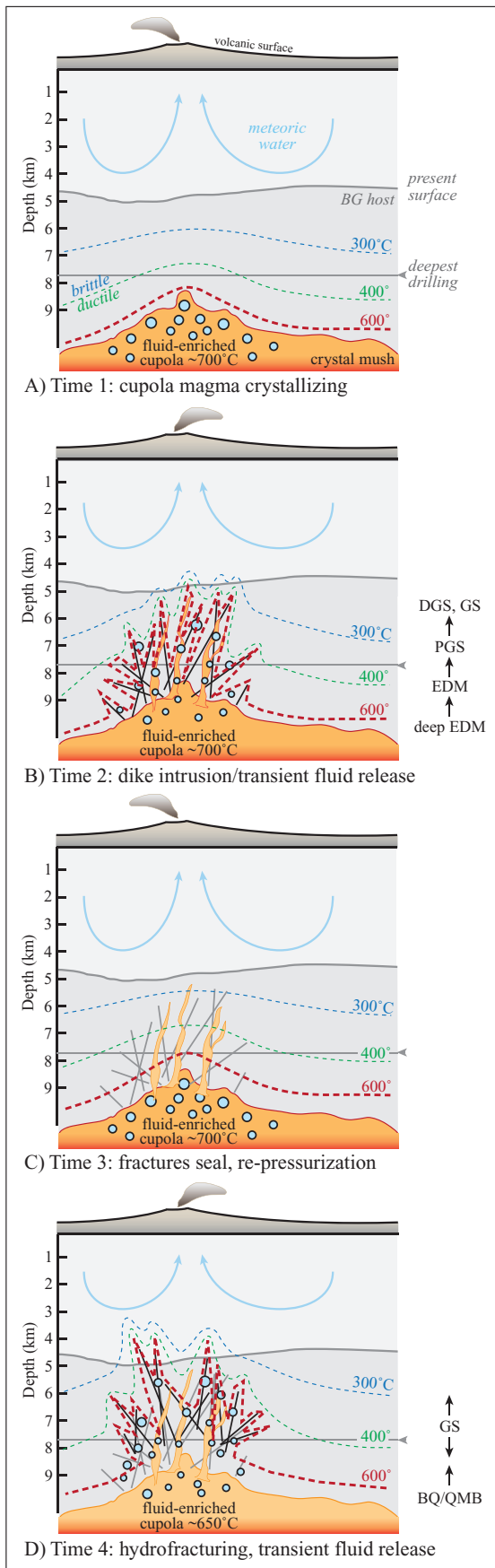
FIG. 16. Pressure-temperature diagram showing the magmatic-hydrothermal continuum. Liquid + vapor saturation curve for an aqueous fluid containing 4 wt % NaCl and 5 mol % CO_2 is shown with a thick gray line. Isochores (g/cm^3) for the same fluids are shown with thin gray lines (Rusk et al., 2008c). Fluid entrapment P-T estimates from Rusk et al. (2008c) are shown by light-colored shaded fields. This study extends the upper limit of temperature estimates for EDM veins (dark-purple shaded field and dashed arrow), PGS veins (green dashed arrow), BQ and QMB veins (dark-blue shaded field and dashed arrow), as well as late-formed GS veins (yellow arrow). The haplogranite water-saturated solidus curve (thick black line) and liquidus curves (thin black lines) for given amounts of H_2O are shown from Holtz et al. (2001). Approximate H_2O -saturation curves for given amounts of H_2O are shown with thin dashed black lines (modified from Holtz and Johannes, 1994). Color-shaded fields at the top of the diagram indicate temperature ranges for the Butte Granite biotite and quartz, the porphyry magmatic quartz, and the inferred maximum bulk host-rock temperature from this study. The orange star shows the approximate P-T conditions of magmatic and hydrothermal overlap where the intrusion of H_2O -saturated porphyry dikes with 25% crystals (Mercer, 2009) would release aqueous fluids that could then be trapped in nearby deep, barren quartz (\pm mb) veins along appropriate isochores. Varying amounts of decompression and cooling of these same fluids leads to EDM, PGS, and GS vein formation as described by Rusk et al. (2008c) and Reed et al. (2013).

approximate the magmatic temperatures that prevailed during dike injection and fluid release (Figs. 16, 17). These high temperatures exceed previous estimates (Rusk et al., 2008c) for EDM and BQ veins by $\sim 50^\circ\text{C}$.

These same veins have minimum temperatures of $\sim 450^\circ$ to 500°C , which we interpret as the upper limits for the Butte Granite host-rock temperature during vein formation, given that hydrothermal veins cannot cool below ambient wall-rock temperatures (Figs. 16, 17). Assuming a geothermal gradient of $45^\circ\text{C}/\text{km}$ for a hot magmatic arc (e.g., Rothstein and Manning, 2003) and a deposit formation depth of approximately 9 km (Dilles et al., 1999; Rusk et al., 2008c), we expect a background crustal temperature of $\sim 400^\circ\text{C}$. The maximum host-rock temperature we infer from hydrothermal veins is $\sim 50^\circ$ to 100°C higher than this estimated background crustal temperature, which is consistent with the close proximity to the

metamorphic aureole of the Butte source stock. The temperature range between the magmatic and wall-rock thermal limits, preserved in veins, may record transient thermal conditions related to variable cooling of hot (700°C) fluids upon contact with cooler ($\sim 450^\circ$ – 500°C) wall rock as magmatic-hydrothermal fluids were injected into the crust along hydrofractures.

The hypothesis that the Butte vein minerals captured transient and evolving thermal conditions suggests that vein formation is a short-lived process, a concept further supported by several observations. First, rutile temperature distributions from veins and adjacent alteration envelopes are broad and virtually indistinguishable, which suggests that both vein and envelope formation took place under the same transient thermal conditions. This inferred transient state must have been sustained long enough (e.g., a maximum of 10s of years;



Geiger et al., 2002) to form envelopes, but short enough that a steady-state thermal regime was never established. Second, the preservation of sharp-edged CL textures in quartz from all sample types and depths, especially from early-formed deep samples (Fig. 5C), suggests that the cumulative time any vein spent at high enough temperatures for Ti diffusion to “blur” sharp CL edges (e.g., $>600^{\circ}\text{C}$, due to a long-lived, pervasively high thermal gradient or a long-lived flux of high-temperature fluids) must have been relatively short (Cherniak et al., 2007b; Mercer, 2009). Finally, given an average volcanic arc crust thermal gradient of $45^{\circ}\text{C}/\text{km}$ (Rothstein and Manning, 2003), a sample of any given vein type that formed 2 km deeper than another sample of the same type should yield temperatures that are systematically higher by at least $\sim 90^{\circ}\text{C}$, or even $\sim 150^{\circ}$ to 200°C if a domical thermal profile is applicable. However, our data show no apparent correlation between sample temperature and sample depth for any given vein type within the deposit (Figs. 2, 11), which is difficult to reconcile without invoking a local, transient “spikey” temperature profile. Considering that monogenetic hydrofracturing fluid injections likely extend at least 2 km vertically, as indicated by biotite crackles with vertical extents >2 km, our data indicate that hot, magmatic fluids may reach shallow portions of the system relatively quickly without extensive overall cooling or thermal equilibration before precipitating hydrothermal minerals.

The lack of correlation between sample temperature and sample depth for a given vein type may relate to the timing of hydrofracture propagation, volume, and duration of expelled fluids, and temperature and extent of wall-rock reaction. Reed et al. (2013) present geochemical models for water-rock reactions that demonstrate that a single initial magmatic fluid is

FIG. 17. Schematic diagram outlining our model for the evolution of the thermal profile during the formation of the Butte porphyry Cu-Mo system. (A). At an initial time 1, an upper-crustal plutonic complex has intruded the Butte Granite (BG) host and produced a volatile-rich felsic magma that concentrates sulfur and metals into a cupola. The intrusion produces a contact aureole (dashed lines) that mimics the shape of the host intrusion. Fluid over-pressurization generated within the crystallizing cupola due to fluid exsolution leads to (B) hydrofracturing of the overlying Butte Granite host rock (thin black lines), intrusion of porphyry dikes (thick, orange streaming lines), and expulsion of metal-rich aqueous fluids (blue circles) at magmatic temperatures ($\sim 700^{\circ}\text{C}$) into the overlying host rock that is relatively cooler ($\leq 500^{\circ}\text{C}$). Fluids cool upon contact with the host rock as they ascend through fractures, and vein minerals preserve the transient thermal state of the ascending fluids. (C). Mineral filling of veins seals the once-fractured rock. Transient high vein temperatures dissipate into the cooler wall rock, increasing the bulk wall-rock temperature. Fluid over-pressurization grows again until (D), another episode of transient, high-temperature fluid release occurs (\pm dike intrusions), forming new veins (thin black lines) that cut older veins (thin gray lines). Early in the evolution of the system, as this dynamic process repeats and the brittle-ductile transition ($\sim 400^{\circ}\text{C}$ isotherm) rises, newly formed veins might extend to higher levels within the deposit. During the late stages of the system as the magmatic heat supply wanes, the brittle-ductile transition descends and we expect newly formed veins to extend to deeper levels in the deposit, cutting previous generations of veins with slightly cooler temperatures (e.g., GS veins). Note that at any given time, the high-temperature thermal profile locally follows active fractures and does not mimic domical-shaped isograds that describe different zones of mineralization. Instead the episodic, transient thermal profile resembles the crown on the Statue of Liberty. General distribution of vein types is denoted to the right of the diagrams. BQ = barren quartz, DGS = dark green sericitic, EDM = early dark micaceous, GS = gray sericitic, PGS = pale-green sericitic, QMB = quartz molybdenite.

capable of producing the full array of alteration types observed at Butte. For example, in their model neutral pH, hot ($\sim 600^\circ\text{C}$) fluids can form potassic alteration, but upon cooling ($\leq 500^\circ\text{C}$) those same fluids become acidic due to SO_2 disproportionation and can then promote sericitic alteration. Monogenetic biotite crackle formation demonstrates that early on, hydrofractures propagated fast and far (i.e., >2 km), transferring relatively small amounts of hot ($\leq 700^\circ\text{C}$), neutral-pH magmatic fluids into the cooler crust and formed narrow selvages of potassic alteration at near-lithostatic pressures. Hydrofracturing events that formed EDM veins apparently expelled similarly neutral-pH, hot ($\leq 700^\circ\text{C}$) fluids, but fractures must have stayed open for a longer time and transferred larger volumes of fluid in order to form thicker, EDM veins and envelopes at pressures intermediate between lithostatic and hydrostatic. So by definition, all EDM veins contain alteration assemblages that identify them as uniquely “early dark micaceous” because they experienced water-rock reaction with similar ranges in temperature, pressure, and fluid-flow duration and volume. Thus, regardless of the depth at which an EDM vein was sampled, we should expect minerals within them to record similar temperatures and pressures. If, for example, a fluid that formed an EDM vein cooled on average $\sim 50^\circ\text{C}$, it should promote formation of PGS veins and envelopes. If this same fluid cooled another $\sim 100^\circ\text{C}$ (either upon ascent to more shallow levels, or later in the deposit’s evolution within the cupola) it should become more acidic and form GS veins and envelopes at near-hydrostatic pressures. Thus all GS veins, regardless of their depth within the deposit, should contain minerals that record cooler temperatures and lower pressures than EDM veins (Fig. 11; also Reed et al., 2013, fig. 10). This reasoning is applicable to all hydrothermal vein types at Butte. Of course hydrofracturing that formed BQ and QMB veins must have been relatively shorter lived so as to preclude development of alteration envelopes, but high volumes of hot fluid ($\sim 600^\circ\text{C}$ – 700°C) must have been expelled to precipitate large amounts of quartz, probably dominantly by pressure drop. The hypothesis that one magmatic fluid can yield all of the observed alteration types explains why a correlation between sample temperature and sample depth for a given vein type is lacking despite the general trend that early-formed veins are hotter than late-formed veins. Differences in the alteration type and extent of alteration among stockwork veins must reflect variations in the timing, distance, and duration of hydrofracturing events, and the prevailing transient temperatures and pressures characteristic of the expelled fluids and wall-rock reactions.

This dynamic, transient vein-forming process is consistent with the classic stockwork veining style at Butte. Newly mineralized rock may cool between episodes of hydrofracturing by dissipating heat into the wall rock, followed by repeated brittle fracturing and vein formation events (Fig. 17). “Anomalous” crosscutting relationships (i.e., high-temperature veins that cut low-temperature veins; Seedorff et al., 2005) in our sample suite provide additional evidence for dynamic behavior. We observe that CL-dark quartz is cut by CL-bright quartz, and vice versa (Fig 4). For example, Figure 4C shows the contact between a CL-gray EDM vein (apparent Ti-in-quartz temperature $\sim 540^\circ\text{C}$) that is cut by a CL-bright BQ vein (apparent Ti-in-quartz temperature $\sim 670^\circ\text{C}$). Quartz

CL-brightness and Ti concentration are proportional to quartz temperature where variations in pressure and growth rate are relatively small, thus the anomalous crosscutting relationships identified by CL textures indicate that sequential vein-forming events oscillate between being relatively hot, cold, and then hot again. Rutile temperature data, which are more robust than those derived from quartz, illustrate the same pattern and show that vein temperatures may fluctuate by at least 60°C within a single cubic centimeter of rock from one vein-forming event to the next.

Figure 17 schematically summarizes our hypothesis; we suggest that the temperature spreads we observe in the Butte samples record cycles of transitory, high-temperature (up to $\sim 700^\circ\text{C}$) hydrofracturing, fluid release, and vein formation in a cooler ($\leq 450^\circ\text{C}$ – 500°C) background host-rock thermal regime. With each episode of fluid release, old stockwork veins may be crosscut and new stockwork veins formed. With each subsequent hydrofracturing event, background temperatures may increase slightly in a domical shape about the core of the stockwork, but the larger volume of rock is never pervasively heated to the high temperatures recorded in hydrothermal veins. This model is compatible with multiple episodes of relatively quick fluid expulsion without pervasive heating of the wall rock to near-magmatic temperatures. Indeed as Roberts (1975) pointed out, fresh Butte Granite between stockwork veins that formed upward of 700°C shows no evidence of ubiquitous heating to 700°C . Finally, late evolution of the Butte porphyry deposit is distinguished by a declining heat supply.

Conclusions

Application of the relatively new quartz, rutile, and biotite thermobarometers utilized in this study highlights the importance of having an understanding of thermobarometer limitations for the specific sample suite under investigation. Although Ti concentrations in igneous and hydrothermal quartz vary systematically with quartz textures observed in SEM-CL, application of the Ti-in-quartz thermobarometer of Thomas et al. (2010) produces unreasonably low temperatures for the Butte magmatic-hydrothermal system. Results from the Ti-in-quartz thermobarometer of Huang and Audélat (2012) are reasonable for magmatic and hydrothermal samples and resemble those from Zr in rutile (Tomkins et al., 2007). However, detailed application and interpretation of Ti-in-quartz data is limited, particularly for hydrothermal quartz, owing to expected variability in pressure and quartz growth rate. Further investigation into the complexities of Ti solubility in quartz is warranted (e.g., Wilson et al., 2012). The Zr-in-rutile (Tomkins et al., 2007) and X_{Mg} -Ti-in-biotite (Henry et al., 2005) thermobarometers generate plausible temperatures that agree well with previous independent estimates (Roberts, 1975; Brimhall, 1977; Geiger et al., 2002; Field et al., 2005; Rusk et al., 2008c; Reed et al., 2013), supporting our conclusion that these temperature estimates are the most robust.

Our results provide new temperature estimates for several vein types at Butte, and confirm previous estimates for EDM veins (Roberts, 1975; Brimhall, 1977; Field et al., 2005). All quartz, rutile, and biotite define wide ranges of composition, analogous to other mineral and fluid inclusion data sets from Butte (Field et al., 2005; Rusk et al., 2008c) and other porphyry

Cu deposits (e.g., El Teniente; Rabbia et al., 2009). By treating these ranges as a distribution rather than averaging them, we recognize a magmatic-hydrothermal temperature spectrum displayed among the hydrothermal vein samples, with an overlap in temperatures (650°–700°C) between magmatism and vein formation. The maximum temperatures from early formed veins (~700°C) represent the final dike injection temperature, and the temperature of the exsolved magmatic-hydrothermal fluid, whereas the minimum temperatures indicate that the Butte Granite host rock temperature was ≤500°C. Between these two thermal boundaries, temperatures for distinct mineralization generations within individual veins span 50° to 250°C and record variable cooling of hot magmatic aqueous fluids upon contact with cooler wall rock during fracture filling and vein formation.

We present a new model for the space-time character of the thermal profile at Butte that does not mirror metasomatic isograds and does not result in pervasive heating of the bulk wall rock as has been previously envisioned. Instead, we propose that the Butte porphyry deposit formed by dynamic, transient episodes of hydrofracturing, fluid release, and mineralization, indicating that the thermal profile fluctuated through both time and space, creating an episodic thermal profile reminiscent of the crown on the Statue of Liberty.

Acknowledgments

This research was supported by the National Science Foundation grant EAR-0440198. We thank Adam Soule for contributing biotite electron microprobe analyses used in this study. We acknowledge the use of the University of Oregon's CAMCOR analytical facilities, which were established with federal and state funding. John Donovan and Steve Weimholt generously provided cutting edge microanalytical expertise and creativity. We also thank Dick Berg of Montana Bureau of Mines, and George Burns and Steve Czheura of Montana Resources for essential assistance in access to drill core and geologic data. We are grateful for Josh Roering's helpful discussion concerning statistics and for thoughtful manuscript reviews from Dana Johnston and Paul Wallace. Finally, we thank John Dilles, Brian Rusk, Jay Thomas, Andrew Tomkins, and Edward du Bray, whose constructive reviews greatly improved this manuscript.

REFERENCES

- Barker, C., and Robinson, S.J., 1984, Thermal release of water from natural quartz: *American Mineralogist*, v. 69, p. 1078–1081.
- Bastin, G.F., Loo, F.J.J., Vosters, P.J.C., and Vrolijk, J.W.G.A., 1984, An iterative procedure for the correction of secondary fluorescence effects in electron-probe microanalysis near phase boundaries: *Spectrochimica Acta*, v. 39, p. 1517–1522.
- Bowman, J.R., Parry, W.T., Kropp, W.P., and Kruer, S.A., 1987, Chemical and isotopic evolution of hydrothermal solutions at Bingham, Utah: *ECONOMIC GEOLOGY*, v. 82, p. 395–428.
- Brimhall, G.H., 1973, Mineralogy, texture, and chemistry of early wall rock alteration in the deep underground mines and continental area, Butte District, Montana: Society of Economic Geologists, Butte Field Meeting, Proceedings, p. H1–H5.
- 1977, Early fracture-controlled disseminated mineralization at Butte, Montana: *ECONOMIC GEOLOGY*, v. 72, p. 37–59.
- Cathles, L.M., and Shannon, R., 2007, How potassium silicate alteration suggests the formation of porphyry ore deposits begins with the nearly explosive but barren expulsion of large volumes of magmatic water: *Earth and Planetary Science Letters*, v. 262, p. 92–108.
- Cherniak, D.J., Manchester, J., and Watson, E.B., 2007a, Zr and Hf diffusion in rutile: *Earth and Planetary Science Letters*, v. 261, p. 267–279.
- Cherniak, D.J., Watson, E.B., and Wark, D.A., 2007b, Ti diffusion in quartz: *Chemical Geology*, v. 236, p. 65–74.
- D'lemos, R.S., Kearsley, A.T., Pembroke, J.W., Watt, G.R., and Wright, P., 1997, Complex quartz growth histories in granite revealed by scanning cathodoluminescence techniques: *Geological Magazine*, v. 134, p. 549–552.
- Dall'Agnol, R., Scaillet, B., and Pichavant, M., 1999, An experimental study of a Lower Proterozoic A-type granite from the eastern Amazon craton, Brazil: *Journal of Petrology*, v. 40, p. 1673–1698.
- Dilles, J.H., Reed, M.H., Roberts, S., Zhang, L., and Houston, R., 1999, Early magmatic-hydrothermal features related to porphyry copper mineralization at Butte, Montana [abs.]: *Geological Society of America Abstract with Programs*, v. 31, p. 380–381.
- Dilles, J.H., Martin, M.W., Stein, H., and Rusk, B.G., 2003, Re-Os and U-Pb ages for the Butte copper district, Montana: A short- or long-lived hydrothermal system? [abs.]: *Geological Society of America Abstract with Programs*, v. 35, p. 400.
- Doe, B.R., Tilling, R.I., Hedge, C.E., and Klepper, M.R., 1968, Lead and strontium isotope studies of the Boulder batholith, southwestern Montana: *ECONOMIC GEOLOGY*, v. 63, p. 884–906.
- Donovan, J.J., Lowers, H.A., and Rusk, B.G., 2011, Improved electron probe microanalysis of trace elements in quartz: *American Mineralogist*, v. 96, p. 274–282.
- du Bray, E.A., Aleinikoff, J.N., and Lund, K., 2012, Synthesis of petrographic, geochemical, and isotopic data for the Boulder batholith, southwest Montana: U.S. Geological Survey Professional Paper 1793, 39 p.
- Evans, B.W., 1965, Application of a reaction-rate method to the breakdown equilibria of muscovite and muscovite plus quartz: *American Journal of Science*, v. 263, p. 647–667.
- Ferry, J.M., and Watson, E.B., 2007, New thermodynamic models and revised calibrations for the Ti-in-zircon and Zr-in-rutile thermometers: *Contributions to Mineralogy and Petrology*, v. 154, p. 429–437.
- Field, C.W., Zhang, L., Dilles, J.H., Rye, R.O., and Reed, M.H., 2005, Sulfur and oxygen isotopic record in sulfate and sulfide minerals of early, deep, pre-Main Stage porphyry Cu-Mo and late Main Stage base-metal mineral deposits, Butte district, Montana: *Chemical Geology*, v. 215, p. 61–93.
- Geiger, S., Haggerty, R., Dilles, J., Reed, M.H., and Matthai, S., 2002, New insights from reactive transport modeling: the formation of sericitic vein envelopes during early hydrothermal alteration at Butte, Montana: *Geofluids*, v. 2, p. 185–201.
- Ghiorso, M.S., and Evans, B.W., 2008, Thermodynamics of rhombohedral oxide solid solutions and a revision of the Fe-Ti two-oxide geothermometer and oxygen-barometer: *American Journal of Science*, v. 308, p. 957–1039.
- Götze, J., Plötze, M., and Habermann, D., 2001, Origin, spectral characteristics and practical applications of the cathodoluminescence (CL) of quartz—a review: *Mineralogy and Petrology*, v. 71, p. 225–250.
- Grew, E.S., Yates, M.G., Shearer, C.K., Haggerty, J.J., Sheraton, J.W., and Sandiford, M., 2006, Beryllium and other trace elements in paragneisses and anatectic veins of the ultrahigh-temperature Napier Complex, Enderby Land, East Antarctica: the role of sapphirine: *Journal of Petrology*, v. 47, p. 859–882.
- Griffen, D.T., 1992, *Silicate crystal chemistry*: New York, Oxford University Press, 442 p.
- Hayden, L.A., and Watson, E.B., 2007, Rutile saturation in hydrous siliceous melts and its bearing on Ti-thermometry of quartz and zircon: *Earth and Planetary Science Letters*, v. 258, p. 561–568.
- Henry, D.J., Guidotti, C.V., and Thomson, J.A., 2005, The Ti-saturation surface for low-to-medium pressure metapelitic biotites: Implications for geothermometry and Ti-substitution mechanisms: *American Mineralogist*, v. 90, p. 316–328.
- Holtz, F., and Johannes, W., 1994, Maximum and minimum water contents of granitic melts: Implications for chemical and physical properties of ascending magmas: *Lithos*, v. 23, p. 149–159.
- Holtz, F., Becker, A., Freise, M., and Johannes, W., 2001, The water-undersaturated and dry Qz-Ab-Or system revisited. Experimental results at very low water activities and geological implications: *Contributions to Mineralogy and Petrology*, v. 141, p. 347–357.
- Huang, R., and Audétat, A., 2012, The titanium-in-quartz (TitaniQ) thermobarometer: A critical examination and re-calibration: *Geochimica et Cosmochimica Acta*, doi:10.1016/j.gca.2012.01.009.
- Jiao, S., Guo, J., Mao, Q., and Zhao, R., 2010, Application of Zr-in-rutile thermometry: A case study from ultrahigh-temperature granulites of the

- Khondalite belt, North China craton: Contributions to Mineralogy and Petrology, DOI 10.1007/s00410-010-0602-3.
- Klimm, K., Holtz, F., Johannes, W., and King, P.L., 2003, Fractionation of metaluminous A-type granites: An experimental study of the Wangrah Suite, Lachlan Fold Belt, Australia: *Precambrian Research*, v. 124, p. 327–341.
- Landtwing, M.R., and Pettke, T., 2005, Relationships between SEM-cathodoluminescence response and trace-element compositions of hydrothermal vein quartz: *American Mineralogist*, v. 90, p. 122–131.
- Llovet, X., Pinard, P.T., Donovan, J.J., and Salvat, F., 2012, Secondary fluorescence in electron probe microanalysis of material couples: *Journal of Physics D: Applied Physics*, v. 45, p. 1–22.
- Lund, K., Aleinikoff, J.N., Kunk, M.J., Unruh, D.M., Zeihen, G.D., Hodges, W.C., Du Bray, E.A., and O'Neill, J.M., 2002, SHRIMP U-Pb and ⁴⁰Ar/³⁹Ar age constraints of relating plutonism and mineralization in the Boulder batholith region, Montana: *ECONOMIC GEOLOGY*, v. 97, p. 241–267.
- Lund, K., Aleinikoff, J.N., and Kunk, M.J., 2005, Geochronologic evidence of multiple overlapping, fracture-controlled magmatic and hydrothermal pulses in the Butte district: Genetic implications for Ag and Cu veins and porphyry Mo [abs.]: *Geological Society of America Abstract with Programs*, v. 37, p. 314.
- Mercer, C.N., 2009, Mineralogical indicators of magmatic and hydrothermal processes in continental arc crust: Unpublished Ph.D. dissertation thesis, Eugene, OR, University of Oregon, 177 p.
- Meyer, C., 1965, An early potassic type of wall rock alteration at Butte, Montana: *American Mineralogist*, v. 50, p. 1717–1722.
- Meyer, C., Shea, E.P., and Goddard, C.C., 1968, Ore deposits at Butte, Montana, in Ridge, J.D., eds., *Ore deposits of the United States, 1933-1967: the Graton-Sales volume*, New York, American Institute of Mining, Metallurgical, and Petroleum Engineers, p. 1373–1415.
- Montoya, J.W., and Hemley, J.J., 1975, Activity relations and stabilities in alkali feldspar and mica alteration reactions: *ECONOMIC GEOLOGY*, v. 70, p. 577–583.
- Müller, A., Wiedenbeck, M., van den Kerkhof, A.M., Kronz, A., and Simon, K., 2003, Trace elements in quartz: A combined electron microprobe, secondary ion mass spectrometry, laser-ablation ICP-MS, and cathodoluminescence study: *European Journal of Mineralogy*, v. 15, p. 747–763.
- Müller, A., Herrington, R., Armstrong, R., Seltmann, R., Kirwin, D.J., Stenina, N.G., and Kronz, A., 2010, Trace elements and cathodoluminescence of quartz in stockwork veins of Mongolian porphyry-style deposits: *Mineralium Deposita*, v. 45, p. 707–727.
- Munoz, J.L., and Ludington, S.D., 1974, Fluoride-hydroxyl exchange in biotite: *American Journal of Science*, v. 274, p. 396–413.
- Naney, M.T., 1983, Phase equilibria of rock-forming ferromagnesian silicates in granitic systems: *American Journal of Science*, v. 283, p. 993–1033.
- Rabbia, O.M., Hernández, L.B., French, D.H., King, R.W., and Ayers, J.C., 2009, The El Teniente porphyry-Cu-Mo deposit from a hydrothermal rutile perspective: *Mineralium Deposita*, v. 44, p. 849–866.
- Redmond, P.B., Einaudi, M.T., Inan, E.E., Landtwing, M.R., and Heinrich, C.A., 2004, Copper deposition by fluid cooling in intrusion-centered systems: New insights from the Bingham porphyry ore deposit, Utah: *Geology*, v. 32, p. 217–220.
- Reed, M.H., and Palandri, J., 2010, Ascent and cooling of magmatic fluids: Precipitation of vein and alteration minerals: *London, Water-Rock Interaction*, p. 37–40.
- Reed, M.H., Rusk, B.G., and Palandri, J., 2013, The Butte magmatic-hydrothermal system: One fluid yields all alteration and veins: *ECONOMIC GEOLOGY*, v. 108, p. 1379–1396.
- Richards, J.P., 2003, Tectono-magmatic precursors for porphyry Cu-(Mo-Au) deposit formation: *ECONOMIC GEOLOGY*, v. 98, p. 1515–1533.
- Roberts, S.A., 1973, Pervasive early alteration in the Butte district, Montana: *Society of Economic Geologists, Butte Field Meeting Guidebook, Anaconda Company*, p. HH1–HH8.
- 1975, Early hydrothermal alteration and mineralization in the Butte district, Montana: Unpublished Ph.D. dissertation thesis, Cambridge, MA, Harvard University, 157 p.
- Rothstein, D.A., and Manning, C.E., 2003, Geothermal gradients in continental magmatic arcs: Constraints from the eastern Peninsular Ranges batholith, Baja California, Mexico: *Geological Society of America Special Paper*, v. 374, p. 337–354.
- Rusk, B.G., and Reed, M.H., 2002, Scanning electron microscope-cathodoluminescence analysis of quartz reveals complex growth histories in veins from the Butte porphyry copper deposit, Montana: *Geology*, v. 30, p. 727–730.
- Rusk, B.G., Reed, M.H., Dilles, J.H., and Kent, A.J.R., 2006, Intensity of quartz cathodoluminescence and trace-element content in quartz from the porphyry copper deposit at Butte, Montana: *American Mineralogist*, v. 91, p. 1300–1312.
- Rusk, B.G., Lowers, H.A., and Reed, M.H., 2008a, Trace elements in hydrothermal quartz: Relationships to cathodoluminescent textures and insights into vein formation: *Geology*, v. 36, p. 547–550.
- Rusk, B.G., Miller, B.J., and Reed, M.H., 2008b, Fluid-inclusion evidence for the formation of Main Stage polymetallic base-metal veins, Butte, Montana, USA, in Spencer, J. E., and Titley, S. R., eds., *Ores and orogenesis: Circum-Pacific tectonics, geologic evolution, and ore deposits*, 22: Tucson, Arizona Geological Society, p. 573–581.
- Rusk, B.G., Reed, M.H., and Dilles, J.H., 2008c, Fluid inclusion evidence for magmatic-hydrothermal fluid evolution in the porphyry copper-molybdenum deposit at Butte, Montana: *ECONOMIC GEOLOGY*, v. 103, p. 307–334.
- Seedorff, E., Dilles, J.H., Proffett, J.M., Einaudi, M.T., Surcher, L., Stavast, W. J. A., Johnson, D. A., and Barton, M. D., 2005, Porphyry deposits: Characteristics and origin of hypogene features: *ECONOMIC GEOLOGY 100TH ANNIVERSARY VOLUME*, p. 251–298.
- Shore, M., and Fowler, A.D., 1996, Oscillatory zoning in minerals: A common phenomenon: *Canadian Mineralogist*, v. 34, p. 1111–1126.
- Sillitoe, R.H., 1973, The tops and bottoms of porphyry copper deposits: *ECONOMIC GEOLOGY*, v. 68, p. 799–815.
- 2010, Porphyry copper systems: *ECONOMIC GEOLOGY*, v. 105, p. 3–41.
- Sinclair, W.D., 2007, Porphyry deposits: Mineral deposits of Canada: A synthesis of major deposit-types, district metallogeny, the evolution of geological provinces, and exploration methods: *Geological Association of Canada, Mineral Deposits Division, Special Publication 5*, p. 223–243.
- Singer, D.A., Berger, V.I., and Moring, B.C., 2008, Porphyry copper deposits of the world: Database and grade and tonnage models, U.S. Geological Survey Open-File Report 2008-1155, version 1.0.
- Smedes, H.W., Klepper, M.R., and Tilling, R.I., 1973, The Boulder batholith, Montana (a summary): *Society of Economic Geologists, Butte Field Meeting, Proceedings*, p. E1–E16.
- Thomas, J.B., and Watson, E.B., 2012, Application of the Ti-in-quartz thermobarometer to rutile-free systems. Reply to: a comment on: “TitaniQ under pressure: the effect of pressure and temperature on the solubility of Ti in quartz” by Thomas et al.: *Contributions to Mineralogy and Petrology*, v. 164, p. 369–374.
- Thomas, J.B., Watson, E.B., Spear, F.S., Shemella, P.T., Nayak, S.K., and Lanzirrotti, A., 2010, TitaniQ under pressure: the effect of pressure and temperature on the solubility of Ti in quartz: *Contributions to Mineralogy and Petrology*, v. 160, p. 743–759.
- Thompson, J.B., 1970, Geochemical reaction and open systems: *Geochimica et Cosmochimica Acta*, v. 34, p. 529–551.
- Tilling, R.I., 1973, The Boulder batholith, Montana: Product of two contemporaneous but chemically and isotopically distinct magma series: *Society of Economic Geologists, Butte Field Meeting, Proceedings*, p. C1–C5.
- Tomkins, H.S., Powell, R., and Ellis, J., 2007, The pressure dependence of the zirconium-in-rutile thermometer: *Journal of Metamorphic Geology*, v. 25, p. 703–713.
- Tosdal, R.M., and Richards, J.P., 2001, Magmatic and structural controls on the development of porphyry Cu ± Mo ± Au deposits: *Reviews in Economic Geology*, v. 14, p. 157–181.
- Tukey, J.W., 1977, *Exploratory data analysis*: Reading, MA, Addison-Wesley, 688 p.
- Wark, D.A., and Watson, E.B., 2006, TitaniQ: A titanium-in-quartz geothermometer: *Contributions to Mineralogy and Petrology*, v. 152, p. 743–754.
- Wark, D.A., Hildreth, W., Spear, F.S., Cherniak, D.J., and Watson, E.B., 2007, Pre-eruption recharge of the Bishop magma system: *Geology*, v. 35, p. 235–238.
- Watson, E.B., Wark, D.A., and Thomas, J.B., 2006, Crystallization thermometers for zircon and rutile: *Contributions to Mineralogy and Petrology*, v. 151, p. 413–433.
- Wilson, C., Seward, T.M., Allan, A.S.R., Charlier, B.L.A., and Bello, L., 2012, A comment on: “TitaniQ under pressure: the effect of pressure and temperature on the solubility of Ti in quartz,” by Jay B. Thomas, E. Bruce Watson, Frank S. Spear, Philip T. Shemella, Saroj K. Nayak and Antonio Lanzirrotti: *Contributions to Mineralogy and Petrology*, v. 164, p. 359–368.
- Zhang, L., 2000, Stable isotope investigation of a hydrothermal alteration system; Butte porphyry copper deposit: Unpublished Ph.D. dissertation thesis, Corvallis, OR, Oregon State University, 182 p.